PLANETARY RING DYNAMICS

Matthew Hedman
Cornell University, Ithaca, New York, U.S.A.

Keywords: celestial mechanics, disks, dust, orbits, perturbations, planets, resonances, rings, solar system dynamics

Contents

Summary

1. Introduction to planetary ring systems
2. Orbital perturbations on individual ring particles
   - 2.1 Orbital elements
   - 2.2 Perturbation equations
   - 2.3 Ring-particle responses to specific perturbations
     - 2.3.1 Drag forces
     - 2.3.2 Planetary oblateness
     - 2.3.3 Inertially-fixed forces
     - 2.3.4 Resonant perturbations
3. Inter-particle interactions
   - 3.1 Basic parameters
   - 3.2 Equilibrium particle distributions
     - 3.2.1 Homogeneous rings
     - 3.2.2 Aggregation outside the Roche limit
     - 3.2.3 Self-gravity wakes
     - 3.2.4 Overstable structures and opaque rings
4. External perturbations on dense rings
   - 4.1 Local perturbations
   - 4.2 Resonant perturbations
5. Conclusions

Acknowledgements

Glossary

Bibliography

Summary

Planetary rings provide a natural laboratory for investigating dynamical phenomena. Thanks to their proximity to earth, the rings surrounding the giant planets can be studied at high resolution and in great detail. Indeed, Earth-based observations and spacecraft missions have documented a diverse array of structures in planetary rings produced by both inter-particle interactions and various external perturbations. These features provide numerous opportunities to examine the detailed dynamics of particle-rich disks, and can potentially provide insights into other astrophysical disk systems like galaxies and proto-planetary disks.

This chapter provides a heuristic introduction to the dynamics of the known planetary rings. We begin by reviewing the basic architecture of the four known ring systems surrounding the giant planets. Then we turn our attention to the types of dynamical phenomena observed in the various rings. First, we consider how different forces can modify the orbital properties of individual ring particles. Next, we investigate the patterns and textures generated within a ring by the interactions among the ring particles. Finally, we discuss how these two types of processes can interact to produce structures in dense planetary rings.

1 Introduction to planetary ring systems

Ring systems surround all four of the giant planets in the outer solar system. While all these rings consist of many small particles orbiting their respective planets, the known rings exhibit a wide diversity of structures, and occupy a broad range of dynamical environments. Furthermore, different rings exhibit patterns and features generated by such diverse processes as inter-particle interactions, gravitational perturbations from various satellites, and a number of non-gravitational forces. Hence, before we consider the dynamical phenomena operating in various rings, it is useful to briefly review the properties of the known planetary rings.

As shown in Figure 1, the rings of the giant planets vary dramatically in their structure and their opacity. Opacity is a particularly useful parameter for describing and categorizing rings because it is correlated with such fundamental ring parameters as surface mass density, and because it can be directly measured by observing the amount of light transmitted through or scattered by the rings. Ring opacity is typically quantified using either a transmission coefficient T or an optical depth $\tau = -\ln(T)$. Such parameters depend on the exact path the light takes through the rings, but they can be used to estimate a viewer-independent parameter called the normal optical depth; the optical depth of the ring observed when the light passes perpendicularly through the rings. The normal optical depth of the known planetary rings ranges over more than eight orders of magnitude.

The most extensive and complex ring system belongs to **Saturn**. Furthermore, thanks to the vast amount of data returned by the Cassini spacecraft, Saturn's ring system is now the best-studied in the outer solar system. The most familiar of Saturns

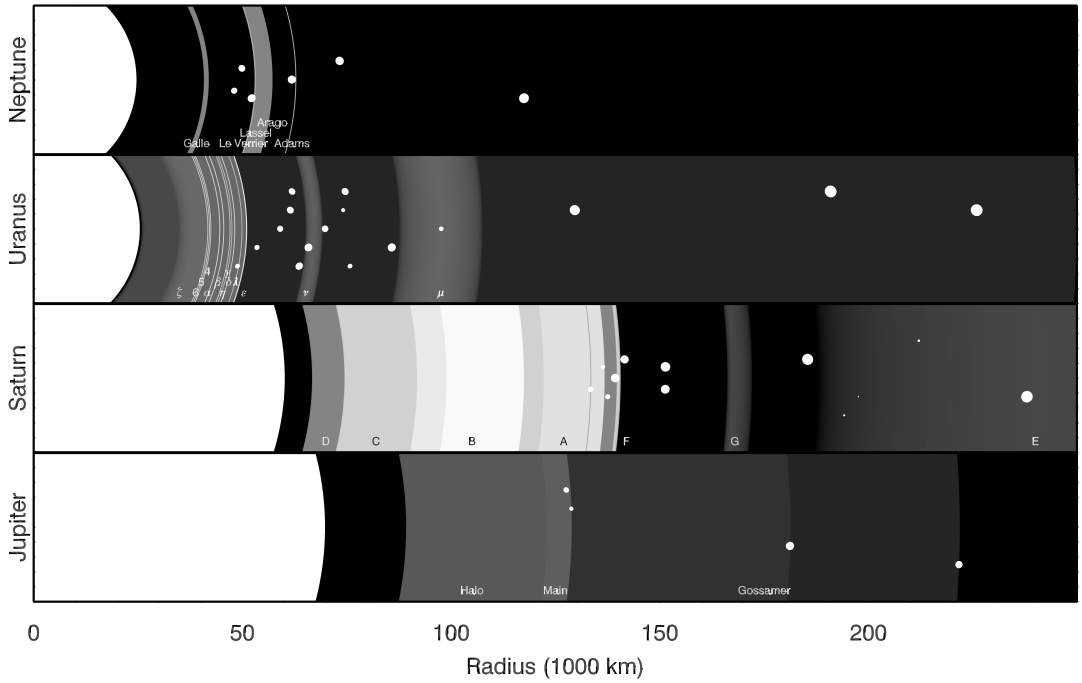

Figure 1: The ring systems of the giant planets, shown to scale. Each grey-scale level corresponds to a decade in ring optical depth. The small white dots correspond to the various moons, with the size of the dots being proportional to the logarithm of their true size. None of these moons are shown to scale with the rings.

rings are the so-called "Main Rings", which include the A, B and C rings, as well as the Cassini Division between the A and B rings. These are all broad rings with substantial optical depths (τ ranging from around 0.1 to over 5) composed of millimeter-to-meter-sized ice-rich particles. Their high opacities and reflectivities makes these rings the easiest ones to see with Earth-based telescopes. Still, it is important to realize that none of these rings are completely homogeneous. Instead, they possess structures on a wide range of scales, and there are even several nearly empty gaps in the A ring, the C ring, and the Cassini Division. Some of these patterns can be attributed to particle-particle interactions or various gravitational perturbations from Saturn's various moons, and therefore provide illustrative examples of the dynamical phenomena that can operate in such dense rings. However, the processes responsible for producing many other structures are still not well understood. Detailed reviews of Saturn's main rings are provided by Colwell *et al.* (2009) and Cuzzi *et al.* (2009).

In addition to these main rings, Saturn also possesses a diverse suite of (mostly) fainter rings, including the D E, F and G rings, some narrow ringlets occupying gaps in the main rings, material in the orbits of various small moons, and the enormous but tenuous disk of debris extending between the orbits of Phoebe and Iapetus. The normal optical depth of these rings ranges from 0.1 for the core of the F ring, to about 10^{-3} for parts of the D ring, to 10^{-6} for both the E and G rings, to as low as 10^{-8} for the extensive Phoebe ring (Horanyi *et al.* 2009, Verbiscer *et al.* 2009). Unlike the dense main rings, the visible appearance of these fainter rings is dominated by dust-sized particles less than 100 microns across. Such small particles are especially sensitive to non-gravitational forces, and so the dynamics of these dusty rings are quite different from those of Saturn's main rings. Horanyi *et al.* (2009) provides a recent review of Saturn's dusty rings.

After Saturn, **Uranus** possesses the most substantial ring system, which is dominated by an array of dense, narrow rings. These rings are designated using either numbers (the 4, 5 and 6 rings) or Greek letters (such as the α, β, γ, δ, ϵ, and η rings). Most of these rings have optical depths between 0.1 and 1.0 and are between 1 and 10 km wide. The exception is the ϵ ring, whose width ranges between 20 and 100 km, and whose optical depth ranges between 0.5 and 2.5. These narrow, dense rings are surrounded by dusty material that has numerous fine-scale structures, including some narrow dusty ringlets like the λ ring. A sheet of dusty material, known as the ζ ring, extends inwards of the dense rings, and two diffuse dusty rings, called the μ and ν rings, have been recently discovered further from the planet (de Pater *et al.* 2006a, b). French *et al.* (1991) and Esposito *et al.* (1991) provide the most recent comprehensive discussions of Uranus' rings, and while the data are still rather limited, several interesting dynamical phenomena have been observed in this system. For example, many of the narrow rings exhibit variations in their widths and radial locations that are due to a combination of perturbations from nearby moons and excited normal modes.

Most of **Neptune**'s dusty rings are rather tenuous, with optical depths around 10^{-3}. The exception is the Adams ring, which contains a series of longitudinally confined arcs with optical depths as high as 0.1. These arcs are of special interest here because they may be confined by a co-rotation resonance with Neptunes small moon Galatea. Porco

et al. (1995) provide a detailed review of Neptune's ring system.

Jupiter's ring system is the most tenuous of all, and appears to be formed primarily of fine debris knocked loose from Jupiters small moons (see Burns *et al.* 2004 for detailed discussions of this system). The so-called Main ring extends interior to the small moons Metis and Adrastea, which are likely to be important sources for the ring material. At the inner edge of the Main ring is the Ring Halo, a vertically extended distribution of debris that likely represents particles whose inclinations have been excited by their interactions with Jupiter's magnetic field. Exterior to the main ring are two extremely faint Gossamer Rings, which appear to be composed of debris knocked off from Amalthea and Thebe. Both these moons are on inclined orbits, and the vertical extent of these structures is consistent with those inclinations.

The structure and dynamics of these planetary rings are due to a diverse array of processes, including interactions among the particles within the rings and external perturbations on the orbits of individual ring particles. Furthermore, many features in the ring actually reflect interactions among multiple dynamical processes. For example, the density waves in Saturn's Main Rings are generated by resonant gravitational perturbations from Saturn's moons, but their propagation through the rings is controlled by collisions and gravitational interactions among the ring particles. Fortunately, there are also features in planetary rings that more clearly document individual dynamical phenomena. In particular, various patterns in the low optical depth rings allow us to demonstrate how external forces can perturb the orbits of individual ring particles, while the small-scale textures of the main rings provide insights into how ring particles interact with each other.

2 Orbital perturbations on individual ring particles

Here we consider how the orbit of an individual ring particle can be perturbed by outside forces. After reviewing the nomenclature for the orbital parameters that will be used in this chapter, we present the generic perturbation equations for these parameters. We will then use these equations to quantify how the ring particles should respond to steady and time-variable (i.e. resonant) perturbations.

2.1 Orbital elements

In the following discussions of ring dynamics, we will use both physical coordinates of ring features and orbital parameters of the component ring particles. For a planetary ring, a cylindrical coordinate system is most natural, so we will designate the location of ring features by their radius r, vertical offset z, and longitude λ. Note that λ is measured relative to a fixed direction in inertial space, so orbiting particles cycle through all possible values of λ once each orbit.

While cylindrical coordinates are a natural basis for describing ring features, the dynamics of these systems are best described in terms of the six classical orbital elements: the semi-major axis a, the eccentricity e, the orbital inclination i, the longitude of as-

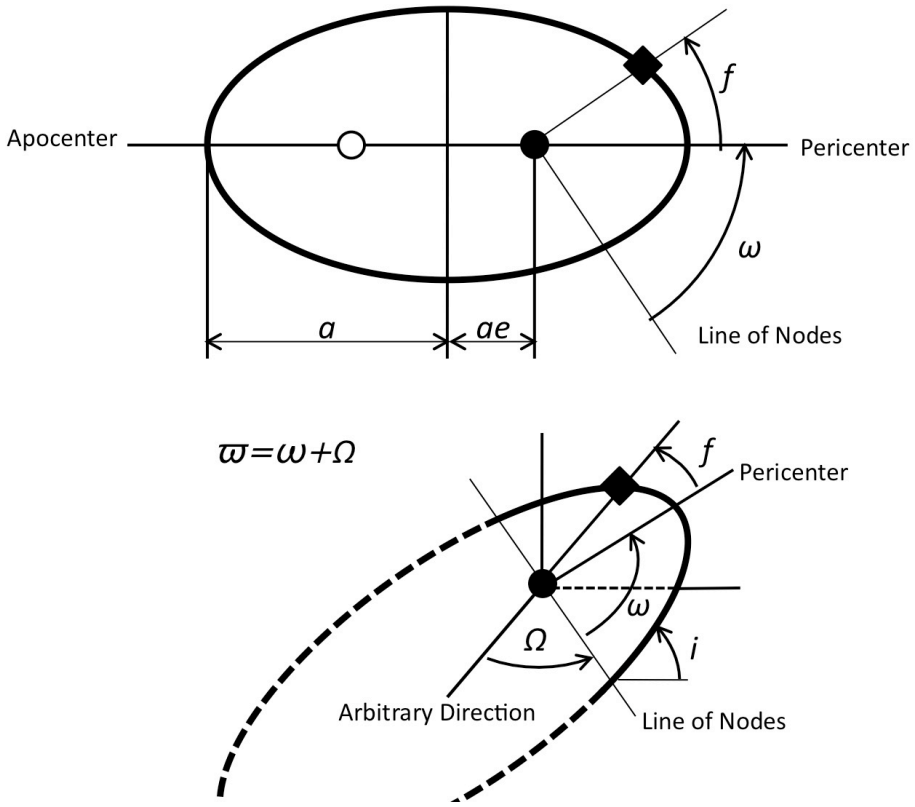

Figure 2: The orbital element nomenclature used in this chapter.

cending node Ω, the argument of pericenter ω and the particles' true anomaly f (Figure 2). The inclination of the ring particles will be measured from the planet's equatorial plane, and Ω is measured from the same inertial direction used to define λ.

Most planetary rings are on very low inclination orbits in this coordinate system, so the longitude of pericenter $\varpi = \Omega + \omega$ is often a more useful parameter than either Ω or ω. In terms of this parameter, the longitude of a ring particle can be written as $\lambda \simeq \Omega + \omega + f = \varpi + f$. Many planetary rings also consist of particles on low-eccentricity orbits, so in the absence of other perturbations, these particles will move around the planet at a rate n that is approximately equal to $(GM_P/a^3)^{1/2}$ where G is the universal gravitational constant, M_P is the planet's mass and a is the orbital semi-major axis.

2.2 Perturbation equations

In addition to the central force from the planet's gravity, ring particles feel various (small) perturbing forces. In general, such a force can be written as: $\vec{F} = F_r\hat{r} + F_\lambda\hat{\lambda} + F_z\hat{z}$, where $\hat{r}$ is a unit vector pointing in the radial direction, $\hat{\lambda}$ is a unit vector pointing in the azimuthal direction, and $\hat{z}$ points normal to the orbit plane. Including such a perturbing force in the appropriate equations of motion yields a series of perturbation equations, which specify how the particles orbital elements should change over time in response to this force. A heuristic derivation of these equations can be found in Burns (1976), and we will not attempt to derive these equations here. Instead, we will simply present the equations, illustrate how they can be simplified for ring particles on nearly circular, low-inclination orbits, and briefly discuss why the resulting expressions are intuitively sensible.

First, let us consider the perturbation equation for the particles semi-major axis:

$$\frac{da}{dt} = \frac{2an}{(1-e^2)^{1/2}}\left[\frac{F_r}{F_G}e\sin f + \frac{F_\lambda}{F_G}(1+e\cos f)\right], \tag{1}$$

where $F_G = GM_Pm/a^2$ is the central force from the planet. The dominant term in this expression is proportional to F_λ/F_G. This makes sense, since a steady force applied along the direction of motion will cause the particle to accelerate, gain energy, and move away from the planet. The other terms involve e, and therefore will be small corrections for most ring particles. However, these terms can still be important in situations where the average azimuthal force applied to the particle over the course of one orbit is zero (e.g. the direction of the force is fixed in inertial space). Thus, even in the limit of a nearly circular orbit ($e << 1$), this equation can only be slightly simplified by approximating $(1-e^2)^{1/2}$ as simply unity:

$$\frac{da}{dt} = 2an\left[\frac{F_r}{F_G}e\sin f + \frac{F_\lambda}{F_G}(1+e\cos f)\right]. \tag{2}$$

Next, consider the perturbation for the particles eccentricity. The general expression is:

$$\frac{de}{dt} = n(1-e^2)^{1/2}\left[\frac{F_r}{F_G}\sin f + \frac{F_\lambda}{F_G}(\cos f + \cos\epsilon)\right], \tag{3}$$

where ϵ is the eccentric anomaly, a quantity that is approximately equal to the true anomaly f for particles on nearly circular orbits considered here. Thus, for typical ring particles we may approximate the above expression as:

$$\frac{de}{dt} = n\left[\frac{F_r}{F_G}\sin f + 2\frac{F_\lambda}{F_G}\cos f\right], \tag{4}$$

In order to verify that this expression is sensible, consider the following: A force that accelerates a particle along the direction of motion near pericenter (i.e. $F_\lambda > 0$ when $f = 0$) causes the eccentricity to grow, while a similar force applied near apocenter (i.e. $F_\lambda > 0$ when $f = 180^\circ$) causes the eccentricity to shrink. Both of these results are consistent with standard orbital dynamics.

The perturbation equation for the orbital inclination is:

$$\frac{di}{dt} = n(1-e^2)^{1/2}\left[\frac{F_z}{F_G}\frac{\cos(\omega+f)}{1+e\cos f}\right], \tag{5}$$

or, in the limit of nearly circular, low-inclination prograde orbits:

$$\frac{di}{dt} = n\left[\frac{F_z}{F_G}\cos(\lambda-\Omega)\right], \tag{6}$$

where we have used the approximate relationship $\lambda \simeq f + \omega + \Omega$, which is valid for low inclinations. Again, we can verify this equation gives sensible results in various simple situations. For example, a vertical force $F_z > 0$ applied when the particle is near its ascending node ($\lambda \simeq \Omega$) and thus already moving northwards, will cause the inclination to grow, while the same force applied near the descending node ($\lambda \simeq \Omega + 180^\circ$) will cause the inclination to shrink.

The perturbation equation for the longitude of ascending node is:

$$\frac{d\Omega}{dt} = \frac{n(1-e^2)^{1/2}}{\sin i}\left[\frac{F_z}{F_G}\frac{\sin(\omega+f)}{1+e\cos f}\right], \tag{7}$$

For nearly circular, low inclination, prograde orbits, this expression becomes:

$$\frac{d\Omega}{dt} = \frac{n}{\sin i}\left[\frac{F_z}{F_G}\sin(\lambda-\Omega)\right], \tag{8}$$

which is a plausible complement to the above perturbation equation for the inclination. For example, a positive vertical force applied when the particle is near its maximum vertical excursion ($\lambda \simeq \Omega + 90^\circ$) will delay the particles' return to the ring-plane and thus move the node longitude forward around the planet.

Finally, we have the following expression for the argument of pericenter:

$$\frac{d\omega}{dt} + \cos i\frac{d\Omega}{dt} = \frac{n(1-e^2)^{1/2}}{e}\left[-\frac{F_r}{F_G}\cos f + \frac{F_\lambda}{F_G}\sin f\frac{(2+e\cos f)}{(1+e\cos f)}\right], \tag{9}$$

For orbits with small e and i, this equation can be transformed into a simpler perturbation equation for the longitude of pericenter $\varpi = \omega + \Omega$:

$$\frac{d\varpi}{dt} = \frac{n}{e}\left[-\frac{F_r}{F_G}\cos f + 2\frac{F_\lambda}{F_G}\sin f\right]. \tag{10}$$

This is a reasonable complement to the perturbation equation for the orbital eccentricity. For example, an outward radial force applied near apocenter ($f \simeq 180°$) will delay the particles' inward motion and thus cause the pericenter to shift forward in longitude.

2.3 Ring-particle responses to specific perturbations

The above equations specify how the ring-particles' orbital parameters will evolve over time in response to any given perturbation. We may now consider specific physical processes, and determine how these phenomena will influence the distributions and motions of ring material. Furthermore, we can compare these predictions with actual structures observed in low-optical-depth rings, where inter-particle interactions can often be ignored.

2.3.1 Drag forces

Drag forces are a useful starting point for these discussions because the dynamical implications of drag are relatively straightforward. A generic drag force will oppose the motion of the ring particles relative to some reference frame, and so one consequence of drag forces is the damping of certain components of the particles velocities. For example, consider a force that damps vertical motion, so $F_z = -D_z v_z$, where D_z is a positive constant and $v_z = ani\cos(\lambda - \Omega)$ is the vertical velocity of the orbiting ring particle. In this case the relevant perturbation equations for the inclination and the ascending node location are:

$$\frac{di}{dt} = -i\frac{an^2 D_z}{F_G}\cos^2(\lambda - \Omega) = -i\frac{D_z}{m}\cos^2(\lambda - \Omega) \tag{11}$$

$$\frac{d\Omega}{dt} = -\frac{an^2 D_z}{F_G}\sin(\lambda - \Omega)\cos(\lambda - \Omega) = -\frac{D_z}{m}\sin(\lambda - \Omega)\cos(\lambda - \Omega) \tag{12}$$

Averaging these expressions over a full orbit yields the following results:

$$\left\langle \frac{di}{dt} \right\rangle = -i\frac{D_z}{2m} \tag{13}$$

$$\left\langle \frac{d\Omega}{dt} \right\rangle = 0 \tag{14}$$

The ascending node therefore does not steadily evolve due to this perturbation, while the inclination is exponentially damped. Similarly, a drag force that opposes radial motions will damp orbital eccentricities. Both these results are physically sensible and demonstrate the utility of the above perturbation equations.

Besides damping inclinations and eccentricities, drag forces can also produce secular evolution in the semi-major axes. Consider a force that opposes azimuthal motion relative a reference frame rotating around the planet at an angular rate n_0. To lowest order, such a drag force is independent of the particles orbital eccentricity and inclination, and the relevant component of the force can be written as $F_\lambda = -F_D(n - n_0)/n_0$. In this limit, the only orbital element with an average non-zero time derivative is the semi-major axis:

$$\left\langle \frac{da}{dt} \right\rangle = -2a \frac{F_D}{F_G} \frac{n}{n_0} (n - n_0). \tag{15}$$

Hence, if $n > n_0$, the semi-major axis will decay over time, while if $n < n_0$, the semi-major axis will grow with time. This again makes sense: if $n > n_0$, then the drag force will act to slow the orbital motion of the ring particles, causing them to spiral inwards towards the planet, while if $n < n_0$, the drag force will accelerate the ring particles and cause them to spiral outwards.

Examples of both inward and outward radial transport due to drag forces can be found in low optical-depth planetary rings associated with small moons. Such rings consist of debris knocked off these small moons by micrometeoroid impacts that is then dispersed by various transport processes, including drag forces. The best-known examples are Jupiter's two Gossamer Rings (Figure 3). Each of these rings has a finite vertical thickness and a distinct "tuna-can" morphology that indicates the particles in these rings have characteristic inclinations similar to that of their likely source moon (either Amalthea or Thebe, Burns *et al.* 1999). More recently, a similar vertical structure has been found in Saturns enormous Phoebe ring, implying that much of the material in this ring has nearly the same orbital inclination as Saturns moon Phoebe (Verbiscer *et al.* 2009). For all of these rings, the ring material is mostly located interior to the relevant moon's semi-major axis, which can be explained as the result of a particular type of drag force called Poynting-Robertson drag, which is a consequence of how these small particles scatter sunlight (Burns, Lamy and Soter 1979). In a reference frame fixed to the Sun, a particle preferentially emits or scatters radiation along its direction of motion, and thus loses forward momentum. Such a drag force corresponds to a case where $n_0 << n$, and thus it always causes the particle to spiral inwards towards the planet.

Other drag forces, however, can cause outward migration. For example, ring particles can exchange momentum with a population of charged subatomic particles trapped in the planets magnetosphere, giving rise to a "plasma drag". The subatomic charged particles are strongly coupled to the planet's magnetic field, and therefore can orbit the planet at rates close to the planet's rotation rate, which exceeds the keplerian orbital rate at sufficiently large semi-major axes. In these situations, $n_0 > n$, and the interactions with the plasma will cause the ring particles to accelerate and thus spiral away from the planet. One place where this process may occur is in Saturn's G ring. This ring extends outwards from the orbit of the small moon Aegaeon, and gets progressively fainter with increasing distance from that moons orbit (see Figure 3). The simplest interpretation of this pattern is that the ring consists of material knocked off from the moon (or other nearby objects), which then drifts outwards due to its interactions with the surrounding

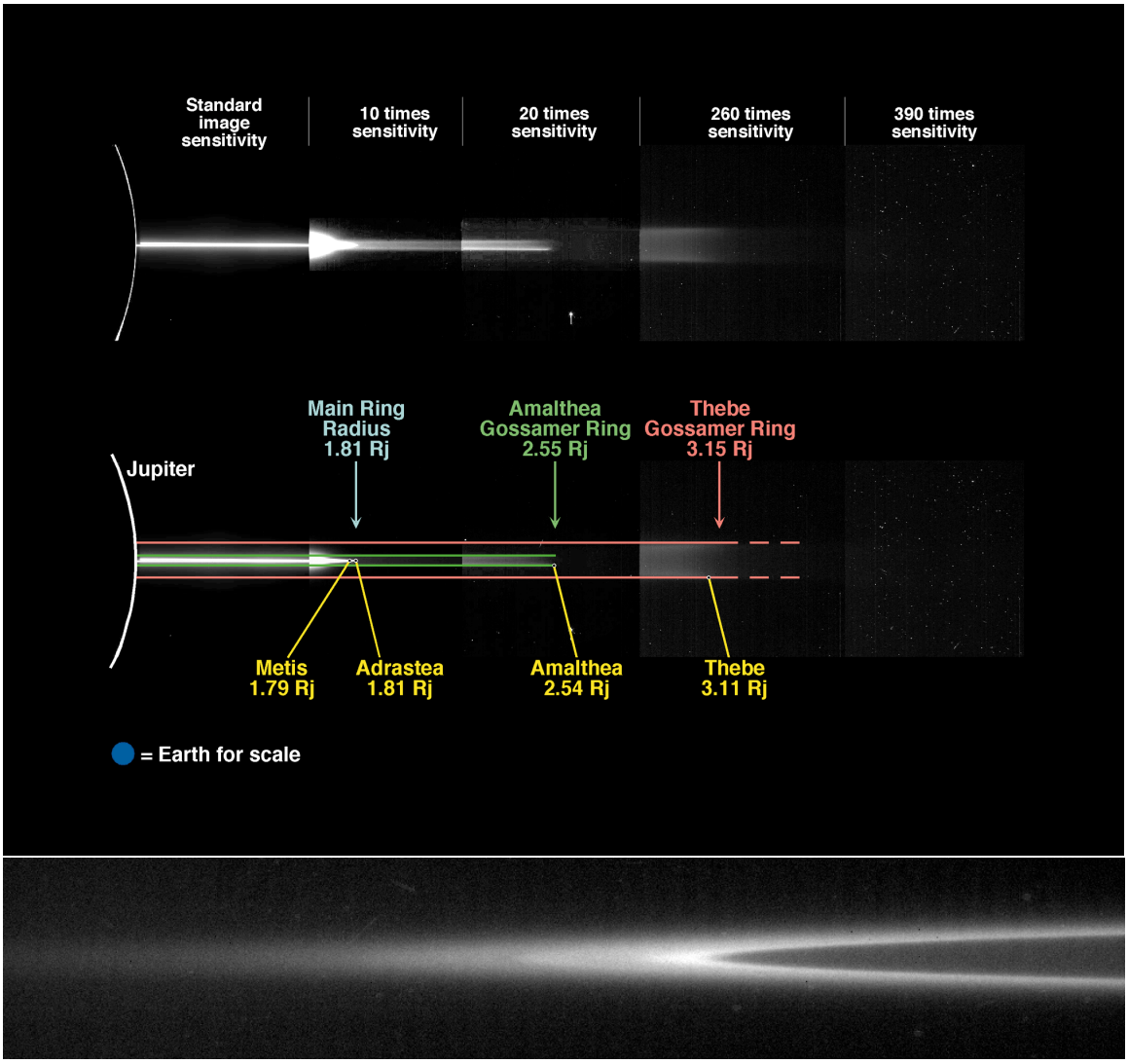

Figure 3: Examples of structures within planetary rings produced by drag forces. Above: Jupiter's two Gossamer Rings appear to consist of material spiraling inwards from the moons Amalthea and Thebe (NASA Planetary Photojournal image PIA01623). Below: Saturn's G ring has an asymmetric profile with a sharp inner edge and a diffuse outer boundary (NASA Planetary Photojournal image PIA07643). Source bodies, including the small moon Aegaeon, have been found near the inner edge of this ring, so much of the material in this ring may consist of material spiraling outward under the influence of plasma drag.

plasma (Hedman *et al.* 2007). A similar process may also be at work in Uranus' μ-ring, which extends outwards from the orbit of Uranus' small moon Mab (de Pater *et al.* 2006b).

2.3.2 Planetary oblateness

Another simple application of the perturbation equations involves particles in orbit around an oblate planet. If a planet has a finite oblateness then the gravitational potential near the equator is given by:

$$U = -\frac{GM_P m}{r}\left[1 - J_2\left(\frac{R}{r}\right)^2\left(\frac{3z^2}{2r^2} - \frac{1}{2}\right)\right]. \tag{16}$$

So long as the oblateness-quantifying parameter J_2 is small, the second term in this expression can be interpreted in terms of a small correction to the planet's apparent mass plus an additional perturbing force. Near the planet's equator the perturbing force has the components:

$$F_r \simeq -3J_2F_G\left(\frac{R}{a}\right)^2 e\cos f, \tag{17}$$

$$F_z \simeq -3J_2F_G\left(\frac{R}{a}\right)^2\frac{z}{a} \simeq -3J_2F_G\left(\frac{R}{a}\right)^2 \sin i \sin(\varpi - \Omega + f). \tag{18}$$

Inserting these expressions into the perturbation equations for a, e and i and averaging over a full orbit only yields small terms of order e and i. Thus the semi-major axis, eccentricity and inclination of the ring particles are not strongly affected by this perturbation. By contrast, the variations in the two angles ϖ and Ω are not so small. Indeed, if we average these perturbations over a single orbit, we obtain the following expressions:

$$\left\langle\frac{d\varpi}{dt}\right\rangle = \frac{3}{2}nJ_2\left(\frac{R}{a}\right)^2, \tag{19}$$

$$\left\langle\frac{d\Omega}{dt}\right\rangle = -\frac{3}{2}nJ_2\left(\frac{R}{a}\right)^2. \tag{20}$$

Thus the planet's oblateness causes the partcle's orbital pericenter to precess and its ascending node to regress around the planet at a rate of order nJ_2. These precession rates are consistent with those derived using the potential directly (see Murray and Dermott 1999).

All the planets with rings have substantial J_2 values, and indeed the orbits of moons and ring particles have pericenters that precess and ascending nodes that regress at detectable rates. These precessional motions have important implications for how the ring particles respond to other perturbations.

2.3.3 Inertially-fixed forces

While the perturbation equations do yield the correct precession rates due to planetary oblateness and sensible radial drifts due to drag forces, the true power of the pertubation equations is that they can be applied to any perturbing force, including ones that have more complex effects on the dynamics of the ring particles. For example, say the ring particle is being perturbed by an outside force that always points in the same direction in inertial space:

$$F_z = +F_I \sin B \tag{21}$$

$$F_r = +F_I \cos B \cos(\lambda - \lambda_0) \tag{22}$$

$$F_\lambda = -F_I \cos B \sin(\lambda - \lambda_0) \tag{23}$$

where B is an elevation angle above the ring-plane and λ_0 is a longitude. Inserting these values into the general perturbation equations in Section 2.2, and noting that $f = \lambda - \varpi$ yields:

$$\frac{da}{dt} = -2an\frac{F_I}{F_G}\cos B[e\sin(\varpi - \lambda_0) + \sin(\lambda - \lambda_0)] \tag{24}$$

$$\frac{de}{dt} = -\frac{n}{2}\frac{F_I}{F_G}\cos B[3\sin(\varpi - \lambda_0) + \sin(2\lambda - \varpi - \lambda_0)] \tag{25}$$

$$\frac{d\varpi}{dt} = -\frac{n}{2e}\frac{F_I}{F_G}\cos B[3\cos(\varpi - \lambda_0) - \cos(2\lambda - \varpi - \lambda_0)] \tag{26}$$

$$\frac{di}{dt} = n\frac{F_I}{F_G}\sin B\cos(\lambda - \Omega) \tag{27}$$

$$\frac{d\Omega}{dt} = \frac{n}{\sin i}\frac{F_I}{F_G}\sin B\sin(\lambda - \Omega) \tag{28}$$

If we assume F_I, λ_0 and B are constants that do not vary over an orbital period, then di/dt and $d\Omega/dt$ will average to zero over an orbit period, while the derivatives of the semi-major axis, eccentricity and pericenter location average to:

$$\left\langle \frac{da}{dt} \right\rangle = -2ane\frac{F_I}{F_G}\cos B\sin(\varpi - \lambda_0) \tag{29}$$

$$\left\langle \frac{de}{dt} \right\rangle = -n\frac{3F_I}{2F_G}\cos B\sin(\varpi - \lambda_0) \tag{30}$$

$$\left\langle \frac{d\varpi}{dt} \right\rangle = -\frac{n}{e}\frac{3F_I}{2F_G}\cos B\cos(\varpi - \lambda_0) \tag{31}$$

Rather than examine this exact set of differential equations, it is more useful to consider equations that also account for the so-called "free precession" in the particle's orbital pericenter due to planet's finite oblateness. This is accomplished by simply adding the term $\dot{\varpi}_0 = 1.5nJ_2(R/a)^2$ to the equation for $\langle d\varpi/dt\rangle$:

$$\left\langle \frac{d\varpi}{dt} \right\rangle = -\frac{n}{e}\frac{3F_I}{2F_G}\cos B\cos(\varpi - \lambda_0) + \dot{\varpi}_0 \tag{32}$$

The advantage of including this constant term is that for any semi-major axis a there is a steady-state solution to Equations 29, 30 and 32 where none of the orbital elements change with time. This steady-state solution has $e = e_f = \frac{3}{2}\frac{n}{\dot{\varpi}_0}\frac{F_I}{F_G}\cos B$ and $\varpi = \lambda_0$. In essence, the perturbing force has broken the rotational symmetry of the system, and the only orbit that can maintain a constant eccentricity has its pericenter aligned with the perturbing force. Of course, this fixed solution is a special case, and more general solutions to the above equations of motion can be found. These solutions are most easily expressed using the variables $h = e\cos(\varpi - \lambda_0)$ and $k = e\sin(\varpi - \lambda_0)$. In terms of these variables, the above equations of motion become:

$$\left\langle \frac{da}{dt} \right\rangle = -\frac{4}{3}a\dot{\varpi}_0 e_f k \tag{33}$$

$$\left\langle \frac{dh}{dt} \right\rangle = -\dot{\varpi}_0 k \tag{34}$$

$$\left\langle \frac{dk}{dt} \right\rangle = \dot{\varpi}_0 (h - e_f) \tag{35}$$

Note that the semi-major axis variations are second order in e and therefore can be neglected. The equations for h and k are just those of two coupled harmonic oscillators. The general solutions to these equations of motion therefore trace out circles in $[h, k]$ space centered on the point $k = 0$ and $h = e_f$. Thus the total eccentricity of the orbit $e = (h^2 + k^2)$ and pericenter location $\varpi = \tan^{-1}(k/h)$ will vary periodically with a frequency $\dot{\varpi}_0$. Indeed, as illustrated in Figure 4, the eccentricity and pericenter position can be modeled as the vector sum in $[h, k]$ space of a constant, or "forced" component e_f and a "free" component e_l with a fixed magnitude but a variable orientation that drifts around at the constant rate $\dot{\varpi}_0$. The magnitude and orientation of the forced eccentricity are determined by the magnitude and direction of the perturbing force, while the magnitude of the free component is set by the initial conditions of the orbit.

Probably the best example of an approximately inertially fixed perturbing force is solar radiation pressure. This is simply the force that arises from solar photons impacting and exchanging momentum with ring particles, which yields a nearly constant anti-sunwards force. According to the above calculations, such a force will yield steady-state orbital solutions where the pericenter is anti-aligned with the Sun. Particles sensitive to this perturbation can therefore give rise to ringlets that counter-intuitively appear to be displaced towards the Sun (see Figure 4). This phenomenon has recently been documented with a faint, low optical depth ringlet in the Cassini Division. This ringlet, which is composed of small (<0.1 mm) particles that are particularly sensitive to non-gravitational forces like solar radiation pressure, is typically found 10 km further from Saturns center at longitudes near the sub-solar side of the planet than it is at longitudes near Saturns shadow (Hedman *et al.* 2010a). These displacements are comparable to the expected radial excursions in the particles' orbits due to solar radiation pressure.

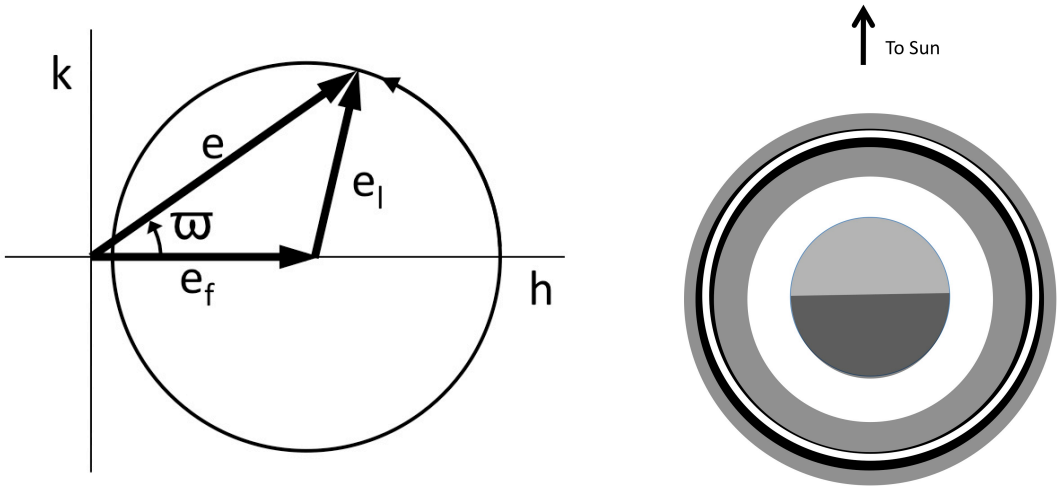

Figure 4: Left: Evolution of a particle's eccentricity and pericenter under the combined influence of precession and a fixed inertial force. Right: Cartoon illustration of the asymmetries in a dusty ringlet caused by solar radiation pressure. The forced eccentricities due to solar radiation pressure cause the center of the ringlet to be displaced from the center of Saturn towards the Sun.

2.3.4 Resonant perturbations

Ring structures generated by perturbation forces with fixed magnitudes and directions like solar radiation pressure are relatively rare. More commonly, features in the rings are generated by forces whose magnitudes and directions vary periodically over time, such as the gravitational pull of a moon. At locations in the rings where the appropriate orbital frequencies are a whole number ratio times the frequency of the periodic force, even small perturbations can have significant effects on the orbital properties of the ring material. These mean-motion resonances are very rich and complex non-linear phenomena, and have been analyzed using a wide variety of sophisticated mathematical techniques (see e.g. Murray and Dermott 1999 and the chapter in this book by Malhotra). However, the basic dynamics of some of the most important resonances in planetary rings can also be understood using the above perturbation equations.

For simplicity, let us first consider a moon of mass M_m on a circular orbit at semi-major axis a_m that lies in the same plane as the rings. In this case, the gravitational pull of the moon on the ring particle has the following components:

$$F_z = 0 \tag{36}$$

$$F_r \simeq +F_m \cos(\lambda - \lambda_m) \tag{37}$$

$$F_\lambda \simeq -F_m \sin(\lambda - \lambda_m) \tag{38}$$

where $F_m = \frac{GM_m m}{a^2 + a_m^2 - 2aa_m \cos(\lambda - \lambda_m)}$ is the magnitude of the gravitational force of the moon on the ring particle and λ_m is the longitude of the moon (Note the above expressions for

the force direction are exact only if $a_m >> a$). Inserting these force components into the perturbation equations for semi-major axis, eccentricity and pericenter longitude ($F_z = 0$ means that the equations for i and Ω are trivial), we obtain the following equations of motion:

$$\frac{da}{dt} = -2an\frac{F_m}{F_G}[e\sin(\varpi - \lambda_m) + \sin(\lambda - \lambda_m)] \tag{39}$$

$$\frac{de}{dt} = -\frac{n}{2}\frac{F_m}{F_G}[3\sin(\varpi - \lambda_m) + \sin(2\lambda - \varpi - \lambda_m)] \tag{40}$$

$$\frac{d\varpi}{dt} = -\frac{n}{2e}\frac{F_m}{F_G}[3\cos(\varpi - \lambda_m) - \cos(2\lambda - \varpi - \lambda_m)] \tag{41}$$

These equations are similar to those derived above for a fixed force. However, it is important to realize that here F_m is an implicit function of $\cos(\lambda - \lambda_m)$, and furthermore λ_m is not a constant, so care is required when averaging these expressions over an orbit.

The force term F_m can be expanded as power series in $\cos(\lambda - \lambda_m)$, so the right hand sides of the above expressions can be written as:

$$\frac{da}{dt} = -2an\frac{M_m}{M_P}\sum_j (e\mathcal{W}_j(a/a_m)\sin[j(\lambda - \lambda_m) - (\lambda - \varpi)] + \mathcal{W}'_j\sin[j(\lambda - \lambda_m)]) \tag{42}$$

$$\frac{de}{dt} = -n\frac{M_m}{M_P}\sum_j \mathcal{X}_j(a/a_m)\sin[j(\lambda - \lambda_m) - (\lambda - \varpi)] \tag{43}$$

$$\frac{d\varpi}{dt} = -\frac{n}{e}\frac{M_m}{M_P}\sum_j \mathcal{X}_j(a/a_m)\cos[j(\lambda - \lambda_m) - (\lambda - \varpi)] \tag{44}$$

Where $\mathcal{W}_j$, $\mathcal{W}'_j$, and $\mathcal{X}_j$ are functions of the semi-major axis ratio a/a_m that we will leave unspecified here for the sake of brevity. For a moon moving on a nearly circular orbit, $\lambda_m = n_m t$, where n_m is the constant mean motion of the moon. Furthermore, so long as the perturbations on the ring particle's orbit are sufficiently small, we can assume that $\lambda \simeq nt$ and $\varpi \simeq \dot{\varpi}_0 t$. Hence, at most locations in the rings, all of the terms in the above equations of motion will average to zero on sufficiently long time scales. Indeed, all of the terms proportional to $\sin[j(\lambda - \lambda_m)]$ in the equation of motion for a will average to zero unless the particle is in nearly the same orbit as the moon.

However, there is an entire set of semi-major axes a_j where for one integer value of j the quantity $j(n - n_m) - (n - \dot{\varpi}_0) \simeq 0$. Each of these locations corresponds to a specific type of resonance known as a first-order **Lindblad resonance**. When a ring particle is near one of these semi-major axes, one of the angles $\varphi_{LR,j} = j(\lambda - \lambda_m) - (\lambda - \varpi)$ is nearly constant, while all of the other terms cycle through 360° on orbital timescales. In this case, the time-averaged equations of motion become:

$$\left\langle \frac{da}{dt} \right\rangle = -2ane\frac{M_m}{M_P}\mathcal{W}_j(a/a_m)\sin\varphi_{LR,j} \tag{45}$$

$$\left\langle \frac{de}{dt} \right\rangle = -n\frac{M_m}{M_P}\mathcal{X}_j(a/a_m)\sin\varphi_{LR,j} \tag{46}$$

$$\left\langle \frac{d\varpi}{dt} \right\rangle = -\frac{n}{e}\frac{M_m}{M_P}\mathcal{X}_j(a/a_m)\cos\varphi_{LR,j} \tag{47}$$

These equations of motion are very similar to the time-averaged equations for a constant force, with the pericenter longitude ϖ replaced by the angle $\varphi_{LR,j}$. As in that previous case, the variations in the semi-major axis will be second order in e and can therefore be ignored. Furthermore, it is again useful to include in the equation of motion for the pericenter location the term arising from the planet's finite oblateness $\dot{\varpi}_0$:

$$\left\langle \frac{de}{dt} \right\rangle = -n\frac{M_m}{M_P}\mathcal{X}_j(a/a_m)\sin\varphi_{LR,j} \tag{48}$$

$$\left\langle \frac{d\varpi}{dt} \right\rangle = -\frac{n}{e}\frac{M_m}{M_P}\mathcal{X}_j(a/a_m)\cos\varphi_{LR,j} + \dot{\varpi}_0 \tag{49}$$

To complete the parallel with the fixed forced case discussed above, we can note that $d\varphi_{LR,j}/dt = j(n-n_m) - (n - d\varpi/dt)$, so we can re-write the second equation as:

$$\left\langle \frac{d\varphi_{LR,j}}{dt} \right\rangle = -\frac{n}{e}\frac{M_m}{M_P}\mathcal{X}_j(a/a_m)\cos\varphi_{LR,j} + \dot{\varphi}_{LR,j0} \tag{50}$$

where $\dot{\varphi}_{LR,j0} = j(n-n_m) - (n-\dot{\varpi}_0)$. For particles with orbital semi-major axes sufficiently close to a_j this angular rate can be written as $\dot{\varphi}_{LR,j0} = -n\frac{\delta a}{a_j}\left[\frac{3}{2}(j-1) + \frac{21}{4}J_2\left(\frac{R}{a_j}\right)^2\right]$, where $\delta a = a - a_j$. Thus, as long as $\delta a \neq 0$, $\dot{\varphi}_{LR,j0}$ will be finite, and there will be a steady-state solution to these equations of motion. This solution has a forced eccentricity:

$$e_f = \frac{n}{|\dot{\varphi}_{LR,j0}|}\frac{M_m}{M_P}\mathcal{X}_j(a/a_m) \tag{51}$$

since $|\dot{\varphi}_{LR,j0}| \propto |\delta a|$, this forced eccentricity diverges as the particles semi-major axis approaches the resonant value a_j.

Meanwhile, the steady-state value of the angle $\varphi_{LR,j}$ is 0 if $\delta a < 0$ and is 180° if $\delta a > 0$. This means that if the particle's semi-major axis lies interior to the resonant location a_j, then the particle will been near pericenter when it has a conjunction with the moon (i.e. when $\lambda = \lambda_m$), and if the particle's semi-major axis lies exterior to the resonant location, then the particle with be near apocenter with it has a conjunction with the moon. Figure 5 illustrates these steady-state trajectories (also called streamlines) in a reference-frame that co-rotates with the moon. In this reference frame, the streamlines form a fixed pattern with j-fold symmetry. Thus even though the particles in this region move at the local orbital rate n, the pattern moves around the planet at the mean motion of the moon $n_m \simeq n(j-1)/j$.

If ring particles were spread throughout this region, then the changing distances between the streamlines will correspond to changes in the apparent surface density of the ring particles. Such patterns have now been observed in several faint rings (Hedman *et al.* 2009a). In denser rings the situation becomes more complicated because particles

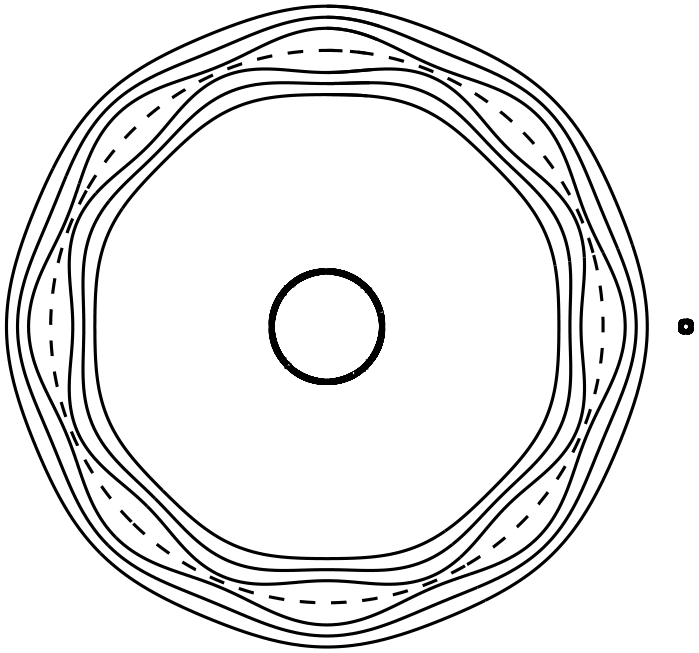

Figure 5: Illustration of the streamlines in the vicinity of a Lindblad resonance with $j = 8$ (also known as the 8:7 inner Lindblad resonance). this diagram uses a reference frame where both the planet and the moon (at right) are fixed, and the steady-state solutions to the ring particle's equations of motion form the closed patterns (not to scale). Note that interior to the resonance location (marked with the dashed line), the particles are near pericenter at conjunction with the moon, while exterior to the resonance, the particles are near apocenter at conjunction. Also note that the pattern is 8-fold symmetric because near this resonance $\lambda - \varpi \simeq j(\lambda - \lambda_m)$ modulo a constant.

can interact with each other through their mutual gravity and collisions, giving rise to features like the density waves described in Section 4.2 below.

Lindblad resonances are just one type of resonance that can influence the structure of planetary rings. Other types of resonances can occur if the moon is not on a perfectly circular, co-planar orbit. For example, if the moon is on a slightly inclined orbit, then the components of the perturbation forces become:

$$F_z = +F_m \sin[i_m \sin(\lambda_m - \Omega_m)] \tag{52}$$

$$F_r = +F_m \cos[i_m \sin(\lambda_m - \Omega_m)] \cos(\lambda - \lambda_m) \tag{53}$$

$$F_\lambda = -F_m \cos[i_m \sin(\lambda_m - \Omega_m)] \sin(\lambda - \lambda_m) \tag{54}$$

where F_m is the same as before, i_m is the moon's inclination and Ω_m is the moon's longitude of ascending node. Assuming $\sin i_m << 1$, then the equations for F_r and F_λ are essentially the same as they would be for the un-inclined case, while the vertical perturbation term becomes:

$$F_z = +F_m i_m \sin(\lambda_m - \Omega_m) \tag{55}$$

In this case, the perturbation equations for the inclination and node position become:

$$\frac{di}{dt} = n i_m \frac{F_m}{F_G} \sin(\lambda_m - \Omega_m) \cos(\lambda - \Omega) \tag{56}$$

$$\frac{d\Omega}{dt} = n \frac{i_m}{i} \frac{F_m i_m}{F_G} \sin(\lambda_m - \Omega_m) \sin(\lambda - \Omega) \tag{57}$$

Once again, we can expand F_m as a power series in $\cos(\lambda - \lambda_m)$. Discarding some terms that will always average to zero if the particle's semi-major axis lies interior to the moons, we obtain the expressions:

$$\frac{di}{dt} = n i_m \frac{M_m}{M_P} \sum_j \mathcal{Y}_j(a/a_m) \sin[(j-1)\lambda - (j+1)\lambda_m + \Omega + \Omega_m] \tag{58}$$

$$\frac{d\Omega}{dt} = -n \frac{i_m}{i} \frac{M_m i_m}{M_P} \sum_j \mathcal{Y}_j(a/a_m) \cos[(j-1)\lambda - (j+1)\lambda_m + \Omega + \Omega_m] \tag{59}$$

These equations have basically the same form as those for eccentricity and pericenter derived above ($\mathcal{Y}_j$ being another unspecified function of the semi-major axis ratio) . Thus again there should be a series of resonant semi-major axes. If a particle has a semi-major axis close to any one of these first-order **vertical resonances**, one of the angles $\varphi_{VR,j} = (j-1)\lambda - (j+1)\lambda_m + \Omega + \Omega_m$ will change slowly with time, and thus the particle's orbit will acquire a forced inclination. The magnitude of the forced inclination diverges as the particles' semi-major axis approaches the resonant radius, and furthermore the ascending node of the steady-state orbit shifts by 180° at the resonant radius.

Such vertical resonances are responsible for features like bending waves and perhaps inclined ringlets in the dense rings (see below). Vertical resonances also play a role in

generating the vertically extended halo in the inner part of Jupiters rings, although in that case the resonance is with periodic variations in the planet's magnetic field rather than with a moon (Burns *et al.* 1985).

Finally, we can consider scenarios where the moon is on an eccentric orbit with eccentricity e_m and pericenter longitude ϖ_m. In this case, the force components have the same form as Equations 36-38 above, but the magnitude of the perturbing force F_m now depends on the true anomaly of the moon $f_m = \lambda_m - \varpi_m$:

$$F_m = \frac{GM_m m}{a^2 + a_m^2[1 - e_m \cos(\lambda_m - \varpi_m)]^2 - 2aa_m[1 - e_m \cos(\lambda_m - \varpi_m)] \cos(\lambda - \lambda_m)} \quad (60)$$

When this expression is expanded to lowest order in e_m one obtains:

$$F_m = \frac{GM_m m}{a^2 + a_m^2 - 2aa_m \cos(\lambda - \lambda_m)} \left[1 + e_m \cos(\lambda_m - \varpi_m) \frac{2a_m^2 - 2aa_m \cos(\lambda - \lambda_m)}{a^2 + a_m^2 - 2aa_m \cos(\lambda - \lambda_m)} \right] \quad (61)$$

The second term is a small correction to the equations of motion for the eccentricity and pericenter longitude, but has a significant effect on the equation of motion for the semi-major axis, because when this term is again expanded as a power series in $\cos(\lambda - \lambda_m)$, it generates a series of terms in the equation of motion for a:

$$\frac{da}{dt} = -2ane_m \frac{M_m}{M_P} \sum_j \mathcal{Z}_j(a/a_m) \sin[j(\lambda - \lambda_m) + (\lambda_m - \varpi_m)], \quad (62)$$

where $\mathcal{Z}_j$ is yet another function of the semi-major axis ratio. Again, there is a series of semi-major axes a_j where one of these terms will be nearly constant in time. At these locations, known as first-order **co-rotation eccentricity resonances**, the semi-major of the ring particle can evolve significantly over time. In particular, we can see that a will evolve to drive the sine of the resonant angle $\varphi_{CR,j} = [j(\lambda - \lambda_m) + (\lambda_m - \varpi_m)]$ towards zero. However, if the semi-major axis changes, then the resonant angle will also begin to change with time. Thus the only steady state solutions are those where $a = a_j$ and $\varphi_{CR,j}$ is either 0 or 180°. Furthermore, if $a < a_m$, only cases where $\varphi_{CR,j} = 180°$ are actually stable to small perturbations. To understand why this is the case, imagine a particle was on an orbit slightly interior to a_j and drifted past the longitude where $\varphi_{CR,j} = 180°$. In this case, the above perturbation would cause the particle's semi-major axis to increase, slowing its mean motion and causing it to drift back towards the point where $\varphi_{CR,j} = 180°$. This kind of resonance can therefore trap material into longitudinally confined arcs of debris.

The clearest examples of material confined by co-rotation resonances are the faint arcs of debris surrounding Saturn's small moons Anthe, Methone and Aegaeon (see Figure 6). The longitudinal extents and mean motions of all these arcs are consistent with them all being material trapped in various co-rotation resonances with Mimas (Hedman *et al.* 2007, 2009b). The arcs in Neptune's Adams ring are also believed to be confined some sort of co-rotation resonance with the moon Galatea (see Figure 6). However, the mean motion of these arcs does not match that predicted for material

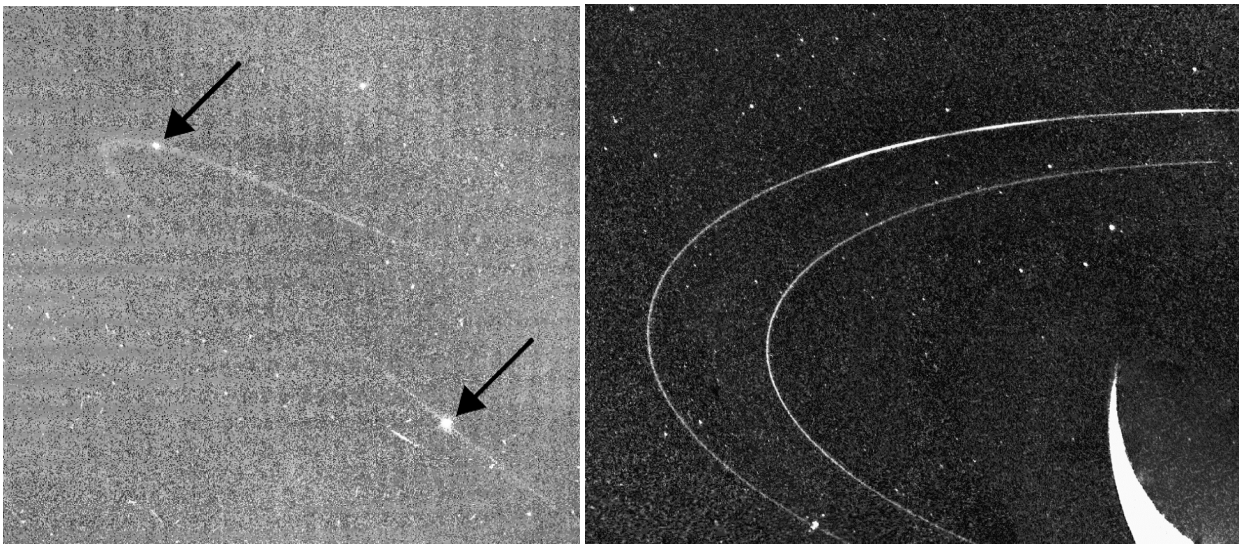

Figure 6: Examples of arc material trapped in planetary rings. Left: Arcs of debris surrounding Saturns moons Anthe and Methone, which are likely confined by resonances with Saturn's moon Mimas (NASA Planetary Photojournal image PIA11102). Right: Arcs in Neptunes Adams Rings, which might be supported by more a more complex resonance with Neptune's moon Galatea (Image from the Voyager Spacecraft obtained from the Planetary Data Service).

in the simple resonance described above. More complex resonances may be involved in producing these arcs, and the mass densities and opacities for the Adams ring could also be sufficiently high that the dynamics of this system are complicated by inter-particle interactions (Porco 1991, Nicholson *et al.* 1995, Dumas *et al.* 1999, Sicardy *et al.* 1999, Namouni and Porco 2002, de Pater *et al.* 2005).

3 Inter-particle interactions

While the most tenuous rings can be treated as a collection of independent ring particles, in denser rings the collisions and gravitational interactions between individual ring particles cannot be ignored. The dynamics of numerous interacting particles are much more complex than the isolated-particles and cannot be so easily described using analytical expressions like those given above. Indeed, numerical simulations now provide some of the most powerful tools for exploring the structure and dynamics of dense rings. Hence, rather than attempt a comprehensive discussion of particle interactions within rings, we will here focus on a few aspects of dense rings that illustrate how collisions and gravitational interactions among ring particles can influence the structure and dynamics of ring material. For more detailed discussions of these and other dynamical phenomena in dense rings, see the recent reviews by Schmidt *et al.* (2009) and Charnoz *et al.* (2009), and the references therein.

3.1 Basic parameters

The physical parameters that are most relevant to the dynamics of interacting ring particles are their sizes (radii) s, their mass densities ρ and their (velocity-dependent) coefficients of restitution ϵ. A real ring will consist of particles with a range of sizes, densities and restitution coefficients, and furthermore these parameters may change with time as collisions cause particles to stick together or break apart. While these processes are important for understanding certain properties of dense rings, they also massively complicate the dynamics. Hence it often useful to consider simpler situations where all the particles have the same size, mass density and surface properties. In such cases, s, ρ and ϵ are treated as independent parameters, with s and ρ being constants, and ϵ being a specified function of impact velocity that is motivated by various experiments (a common choice being $\epsilon = (v/0.0077 \text{ cm/s})^{-0.234}$, which is based on experiments described in Bridges *et al.* 1984).

The dynamical state of a collisional ring also depends the number of particles in the ring. In general the amount of material in a ring region is described by the size distribution of ring particles $d_2(s)$, which specifies the average number of particles of a given size per unit surface area. In the simple case where all the particles have identical sizes, this distribution function reduces to the average number of ring particles per unit surface area, here denoted D_2. In practice, most researchers do not use D_2 itself to describe the total amount of material in the rings, but instead use either the average surface mass density Σ or a quantity known as the dynamical optical depth τ_D. In the case where all particles have the same size and mass density, both the surface mass density and the dynamic optical depth are simple functions of D_2:

$$\Sigma = \frac{4\pi}{3}\rho s^2 D_2, \tag{63}$$

$$\tau_D = \pi s^2 D_2. \tag{64}$$

Even if the particles have a range of sizes, these parameters can be easily derived as the appropriate integrals over the size distribution.

It is important to realize that while Σ is the average surface mass density of the ring, τ_D is not necessarily equal to the normal optical depth observed by any experiment. The above expression assumes that each ring particle obscures an area equal to its cross section, and thus neglects the possibility that a given line of sight can pass through two or more ring particles. Hence, while τ_D is close to the ring's actual observed normal optical depth when $\tau << 1$, the observed τ can deviate significantly from τ_D when the density of the ring is fairly high. Thus τ_D is better understood as a conventional representation of the particle number density, and not an estimate of the actual ring opacity.

Finally, the dynamics of collisional rings depends upon how far the ring is situated from the planet center r.

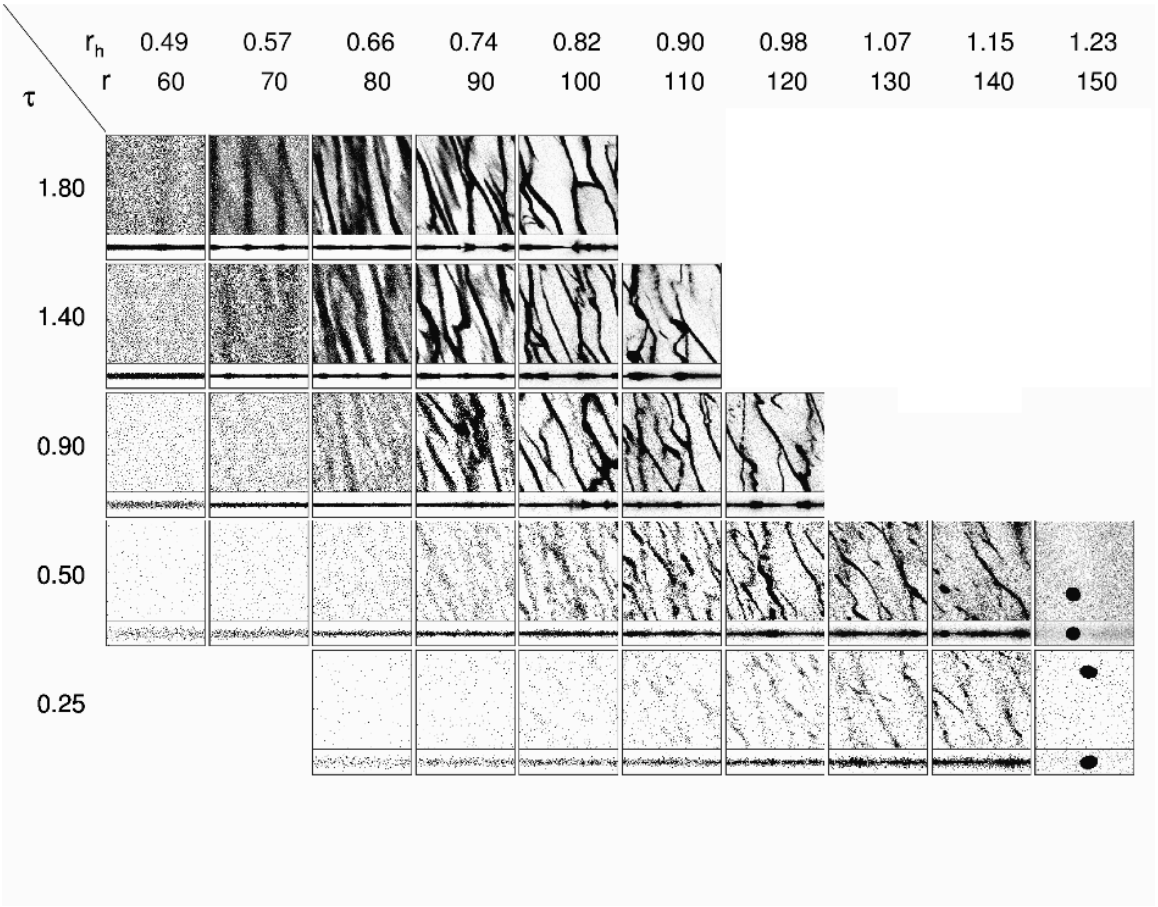

Figure 7: Variations in the structure of dense rings as a function of radius and dynamical optical depth. Each panel shows two simulated views of a small patch of rings, one from above and one from the side (in both plots radius increases to the right). These simulations were computed for rings around Saturn, and the dynamical optical depths of the simulations are given at the far left, while the assumed ring radii r are given along the top (in this plot, $r_h = r/r_H$, where r_H is the Roche Limit for these particles). Figure adapted from Figure 14.7 in Schmidt *et al.* (2009) and kindly provided by H. Salo.

3.2 Equilibrium particle distributions

So long as the ring is unperturbed by outside forces, the average distribution of particles within the ring should depend just on a rather small number of parameters r, s, ρ, ϵ, and D_2 (or equivalently τ_D or Σ). However, even in cases where the particles are all identical, the spatial distribution of ring material is not necessarily simple or homogeneous. Figure 7 shows the results of numerical simulations of small patches within the rings for different values of r and τ_D. This diagram illustrates the various types of structures that can arise just from the interactions among ring particle, which can be divided roughly into four basic classes:

- Situations where the particles are distributed homogeneously, which occur when the surface mass density is low and the ring material is located sufficiently close to the planet (corresponding to the left side and bottom edge of Figure 7).
- Situations where the particles aggregate into large, isolated objects, which occur whenever the ring material is sufficiently far from the planet (corresponding to the right edge of Figure 7).
- Situations where the particles aggregate into long canted structures known as "self-gravity wakes", which occur at moderate to high surface mass densities and at intermediate distances from the planet.
- Situations where the density of the particles develops periodic azimuthal variations in surface mass densities, which occur at high surface mass densities (parts of the top row in Figure 7).

The boundaries between these four regimes are not perfectly sharp, and the extent of these regions depend on the assumed values of s, ρ and ϵ.

3.2.1 Homogeneous rings

The spatial distribution of ring material is fairly homogeneous in the limit where the gravitational interactions among the ring particles can be neglected. In this case, the dynamical state of the rings can be quantified in terms of the root-mean-square velocity dispersion c, which quantifies the magnitude of the random motions within the ring.

Say a ring particle has the velocity components, v_r, v_λ and v_z. These velocities can in turn be decomposed into two parts: the average velocity of all the ring particles within a given small patch of ring (denoted V_r, V_λ and V_z) and the random velocities of the individual ring particles around this mean velocity (denoted here u_r, u_λ and u_z). So long as the ring as a whole does not have a finite eccentricity or inclination, $V_\lambda \simeq nr$, while V_r and V_z are effectively zero. In terms of these parameters, the root-mean-square velocity dispersion is given by the expression $c = \sqrt{\langle u_r^2 \rangle + \langle u_\lambda^2 \rangle + \langle u_z^2 \rangle}$.

This velocity dispersion not only quantifies how fast the ring particles are moving relative to each other, it also determines the vertical thickness of the ring H. Conventionally, a rings thickness is defined in terms of the root-mean-squared value of z for all the

particles in the ring: $H^2 = 12\langle z^2 \rangle$. The factor of 12 in this definition for H ensures that a vertically homogeneous distribution of ring particles has the correct thickness (Salo 2001). Since particles can only be displaced above or below the ring-plane because they are on inclined orbits, there is a direct relationship between the mean-squared vertical positions and mean-squared vertical velocities $n^2\langle z^2 \rangle = \langle u_z^2 \rangle$. Thus, the thickness of the ring H can be written as a simple function of the root mean squared vertical velocity c_z: $H = \sqrt{12}(c_z/n)$. This is also equivalent to $H \sim 2c/n$ if the distribution of random velocities is approximately isotropic, but this is rarely the case in dense rings (Schmidt *et al.* 2009 and references therein).

The equilibrium value of c depends upon how quickly random motions are generated and dissipated by the interactions among the ring particles. Obviously, inelastic collisions will tend to dissipate the random motions of ring particles at a rate which depends on the collision frequency ω_c, and the coefficient of restitution ϵ:

$$\frac{dc^2}{dt} \propto -\omega_c c^2 (1 - \epsilon^2) \tag{65}$$

For sufficiently low optical depth rings, the collision frequency ω_c is $n\tau$ times a numerical constant of order unity, so this dissipation rate is of order $n\tau(1 - \epsilon^2)$.

While inelastic collisions dissipate random motions, collisions among particles with different semi-major axes can actually generate them. To see how this can happen, imagine two ring particles initially moving on perfectly circular orbits with slightly different semi-major axes, with particle 1 having the semi-major axis a_1 and particle 2 having the semi-major axis $a_2 = a_1 + \delta a > a_1$. Furthemore, say that δa is less than the particle diameter $2s$, so the particles can still collide with each other. Since particle 1 has a smaller semi-major axis, it will be moving faster than particle 2 and so particle 1 will naturally tend to collide with particle 2 from behind. The resulting exchange of momentum will therefore tend to decelerate particle 1 and accelerate particle 2, which will cause the semi-major axes of the two particles to diverge. At the same time, particle 1 will be pushed inwards while particle 2 is pushed outwards, producing random motions of the ring particles comparable to the initial difference in their orbital velocities $\delta V_\lambda \sim ns$. The rate at which the random motions will increase by this process can therefore be roughly estimated as:

$$\frac{dc^2}{dt} \propto \omega_c \delta V_\lambda^2 \sim \tau n (sn)^2 \tag{66}$$

If the particles are already on non-circular orbits, then further excitation of random motions is possible. Say there are two particles with semi-major axes that differ by δa, but which have eccentricities $e \sim \delta a/a$, so they can collide when one particle is near periapse and the other is near apoapse. At this location, the two particles will be moving azimuthally at a relative speed $\delta V_\lambda \sim eV_\lambda$. It we neglect dissipation in this collision, then the total orbital energy and orbital angular momentum of the particles must be conserved. However, the direction of particle motion will have changed, and this can lead to changes in both the semi-major axes and the eccentricities of the particles' orbits. In general, the initial trajectories of the particles after the collision are unlikely to

be perfectly azimuthal. This requires that the particles are no longer at their pericenter or apocenter, implying the particles semi-major axes have converged and/or that their eccentricities have increased. Indeed, in order to conserve angular momentum and energy, any excitation of radial motions must increase the eccentricity by an amount δe that is of order the particles eccentricity before the collision. Since the velocity dispersion c is proportional to the eccentricity of the particles' orbits, each of these collisions increases the random motions by a factor of order c. Hence this process excites random motions at a rate given by:

$$\frac{dc^2}{dt} \propto \omega_c c^2 \sim \tau n c^2. \tag{67}$$

Note this expression is only valid for low optical depths: if the optical depth exceeds unity, then the particles cannot complete a full epicycle before a collision, and the efficiency of this process is reduced.

For both of the above processes, random motions are being excited by Keplerian shear, so the energy of random motions is being extracted from the background shear flow of the ring. These processes can therefore be thought of as giving the ring an effective kinematic shear viscosity $\nu_{\rm eff}$. Indeed both the above terms are often expressed in this language:

$$\frac{dc^2}{dt} \propto +\nu_{\rm eff}\left(\frac{dV_\lambda}{dr}\right)^2 \sim \nu_{\rm eff} n^2, \tag{68}$$

where $\nu_{\rm eff} \sim \tau(k_1(c^2/n) + k_2(s^2 n))$, and k_1 and k_2 are coefficients of order unity.

In any case, the dissipation rate will equal the excitation rate at equilibrium, so the equilibrium value of c in a low-optical depth ring is given by the condition: $k_3\omega_c c^2(1-\epsilon^2) = k_1\omega_c c^2 + k_2\omega_c(ns)^2$ which corresponds to:

$$c^2 = \frac{k_2(ns)^2}{k_3(1-\epsilon^2) - k_1}. \tag{69}$$

This expression is only sensible if the denominator is positive (i.e. the coefficient of restitution is sufficiently small). Otherwise, the ring cannot reach a stable equilibrium state. If an equilibrium state exists, then c will be order ns, and the ring will only be a few particle diameters thick.

Note that in this simplistic analysis, c does not depend on optical depth, so we might not expect parameters like the vertical thickness of the ring to vary much with τ. However, as τ approaches 1, the effective viscosity due to particles colliding at different epicyclic phases will decrease, which tends to reduce the equilibrium velocity dispersions (Schmidt *et al.* 2009). However, at this point the gravitational interactions of the ring particles cannot be ignored, so we consider these processes next.

3.2.2 Aggregation outside the Roche limit

The gravitational interactions among the ring particles have the most dramatic affect on the structure of the ring at large distances from the planet. In Figure 7, the particles in

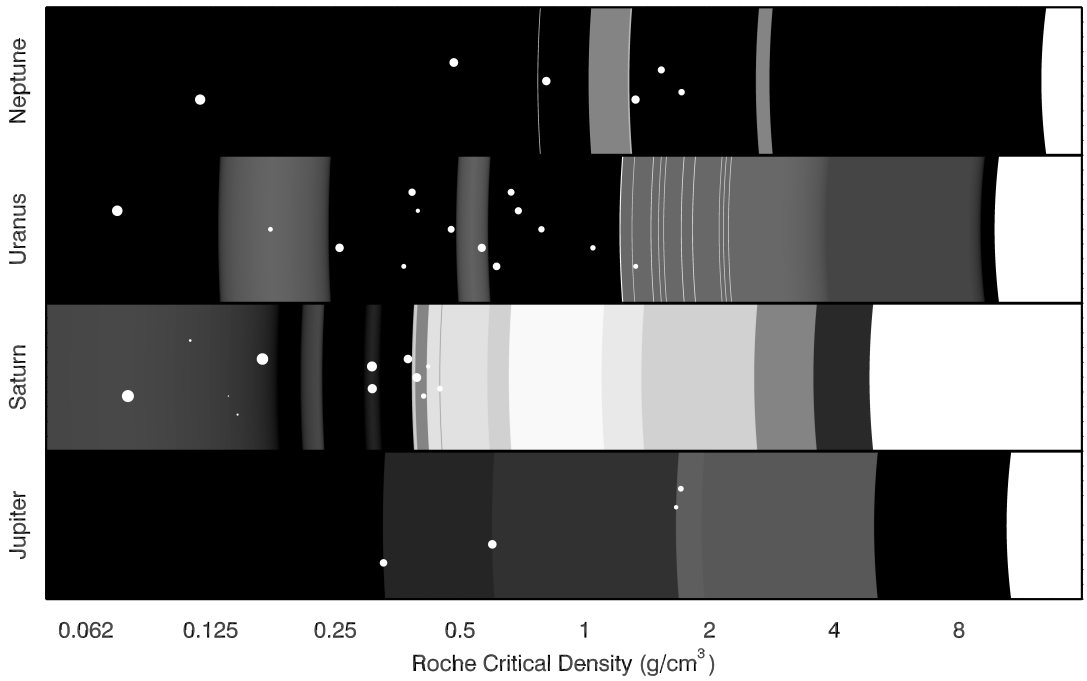

Figure 8: The ring systems of the giant planets plotted as a function of the Roche critical density, assuming $\gamma = 1.6$ (see text).

the simulations with the largest values of r aggregate into moonlets rather than remain dispersed as a ring. These aggregates form beyond a critical distance from the planet's center known as the Roche limit, where the difference in orbital velocities between two particles that are in contact with each other $\delta V_\lambda \sim ns$ roughly equals their mutual escape speed $V_{\rm esc} \sim s\sqrt{G\rho}$. Outside of the Roche limit $\delta V_\lambda < V_{\rm esc}$, so particles that inelastically collide with each other can emerge from the collision with insufficient velocity to escape each other's gravity, hence the two particles remain bound together and orbit the planet as a unit. As time goes on, more and more particles can aggregate together until all of the available ring material has collected into a single body.

The location of the Roche limit r_R can be estimated by setting $\delta V_\lambda \sim V_{\rm esc}$ and solving for the radius r:

$$r_R = \chi R \left(\frac{\rho_P}{\rho} \right)^{1/3} \tag{70}$$

where χ is a number of order unity, R_P is the planets radius, ρ_P is the planet's mean density, and ρ is the mass density of the ring particles. Note that this distance only depends on the particles' mass density, not on their size. Hence for any radial location in the ring r, we can define a Roche critical density $\rho_{\rm crit}$, such that particles with mass densities higher than $\rho_{\rm crit}$ will aggregate into moons, while material with lower mass densities will remain as dispersed rings. Re-arranging the above expression for the Roche Limit yields the following expression for the Roche critical density

$$\rho_{\rm crit} = \frac{3}{\gamma} \frac{M_P}{r^3} \tag{71}$$

where γ is a constant of order unity that depends on the nature of the material (i.e. solid or liquid) and the object's shape.

Figure 8 shows the various ring systems plotted as a function of $\rho_{\rm crit}$. For both Uranus and Saturn (the two planets with extensive dense ring systems) there is a rather sharp transition between the region near the planet occupied by the dense rings and the zone further from the planet occupied by many small moons. In the Saturn system, this transition occurs where the Roche critical density is around 0.5 g/cm^3, which is comparable to the densities of many of Saturns small moons, and is consistent with many of these objects being loose aggregates of ice-rich particles (Porco *et al.* 2007, Charnoz *et al.* 2007). These moons may even have emerged from the spreading rings (Charnoz *et al.* 2010). Intriguingly, the same transition in the Uranus system occurs where the Roche critical density is between 1.0 and 1.5 g/cm^3, which could indicate that Uranus' rings and small moons may be made of denser material than Saturn's (Tiscareno *et al.* 2012). By contrast, Jupiter and Neptune do not show such a clear separation between rings and moons. Instead, most of the rings are found in regions also occupied by moons. This makes the rings of Neptune and Jupiter more like the dusty, faint components of Uranus' and Saturn's ring systems. The distribution of these more tenuous rings is not so strongly controlled by the Roche Limit because they are formed from material launched at finite speeds from various objects by micrometeoroid impacts

etc., and various transport processes like drag forces keep the small particles in these rings from re-aggregating.

3.2.3 Self-gravity wakes

Interior to the Roche limit, the Keplerian shear across the disk prevents the ring particles from collecting into small moons. However, the mutual gravitational attraction among the ring particles still has important effects on the ring's fine-scale texture. In particular, many of the simulations in Figure 7 exhibit elongated agglomerations of particles known as "self-gravity wakes". These structures are transient, constantly forming and disintegrating as particles attempt to clump together under their own gravity but are then pulled apart by Keplerian shear. Nevertheless, the overall pattern is stable: the long axes of the aggregates are always tilted about 20° from the azimuthal direction, and the average perpendicular distance between two adjacent aggregates is typically of order one to a few hundred meters, depending on the assumed surface mass density (see Schmidt *et al.* 2009 and references therein).

The characteristic orientation of these structures is typical of many disturbances in planetary rings, As discussed in detail in Section 4.1 below, gravitational perturbations from nearby massive objects give rise to coordinated ring-particle motions that in turn lead to density variations in the ring material. In particular, at a radial distance δa from the perturbing mass, the first density maximum occurs roughly at a distance between $3\pi\delta a/4$ and $3\pi\delta a/2$ downstream from the mass. This density maximum, or "wake", is therefore canted between $\tan^{-1}(4/3\pi) \sim 24°$ and $\tan^{-1}(2/3\pi) \sim 12°$ from the azimuthal direction, comparable to the orientation observed in the simulated structures. These features can therefore be interpreted as many superimposed wakes surrounding each ring particle. The gravitational interactions among these wakes reinforce these structures and their exact orientation depends on the ring's surface mass density and particle size distribution (Salo *et al.* 2004).

The characteristic scale of these structures is consistent with those expected for certain instabilities within particle-rich self-gravitating disks first investigated by Julian and Toomre (1966) in the context of galactic disks. Specifically, the average perpendicular distance between adjacent density maxima is comparable to the Toomre critical wavelength

$$\lambda_T = 4\pi^2 G\Sigma/n^2, \tag{72}$$

which is the largest unstable wavelength in the shearing disk. Density variations on scales larger than this are destroyed by the shear across the disk, while smaller-scale textures are smoothed out by the random motions of the particles (see also Schmidt *et al.* 2009).

In the known planetary rings, these oriented particle aggregates are of order one hundred meters wide and are therefore too small to be directly imaged by spacecraft. However, they have numerous effects on the average opacity and reflectivity of the rings that can be detected. In particular, the brightness and optical depth of Saturn's A and inner B rings have been observed to vary dramatically with longitude relative to the observer in ways that can be most easily explained as the result of these wakes being

viewed at different angles at different locations within the rings (see Colwell *et al.* 2009 and references therein). These asymmetries therefore can therefore provide useful insights into the particle-level structure of the rings.

3.2.4 Overstable structures and opaque rings

In the highest-density simulations in Figure 7, one can see density variations that are perfectly aligned with the local azimuthal direction. These structures appear to represent a phenomenon known as an "overstability" in the ring material. Unlike an instability, where material collects in more dense regions and so any small density variation grows with time, an overstability occurs when ring particles are being pushed out of overdense regions and into underdense regions too rapidly. In this case, any small density fluctuation yields oscillations of material moving in an out of more dense regions, and the *amplitude* of these oscillations grows with time (Schmidt *et al.* 2009). The detailed dynamics of these structures are still not fully understood. For example, it is not yet clear what ultimately determines the wavelength of these patterns.

At several locations within the inner A and inner B rings, where the normal optical depth is close to unity, there is evidence for highly periodic structures with a characteristic wavelength of order a few hundred meters (Thomson *et al.* 2007, Colwell *et al.* 2007). The wavelengths of these structures are close to those seen in simulated overstable features, but further analysis is needed to fully understand the nature and dynamics of these particular features and to demonstrate that they in fact represent overstable structures.

The overstable regime is not the ultimate limit of dense rings. The B ring has been found to be nearly opaque, with normal optical depths exceeding 5. Such opaque rings lie beyond the range of current numerical simulations (Robbins *et al.* 2010), so the configuration of the particles in these regions remains a mystery. It is even possible that in these regions the ring particles are in constant contact, acting more like a liquid or a solid than like a particulate gas (Tremaine 2003).

4 External perturbations on dense rings

When dense rings are subject to external perturbations, such as gravitational forces from nearby or distant moons, the ring particles respond not only to the perturbing force, but also to the other ring particles in their vicinity. The interactions among particles can cause the coordinated motions to dissipate or allow disturbances to propagate through the ring. The resulting structures are therefore sensitive to both the nature of the perturbation and the physical properties of the rings. Again, a full description of these complex systems is well beyond the scope of this brief introduction, so we will instead simply describe some of the most obvious and well-studied phenomena that occur when dense rings are perturbed by gravitational interactions with nearby and distant satellites. For more details, see such works as Goldreich and Tremaine 1982, Shu 1984 and Murray and Dermott 1999.

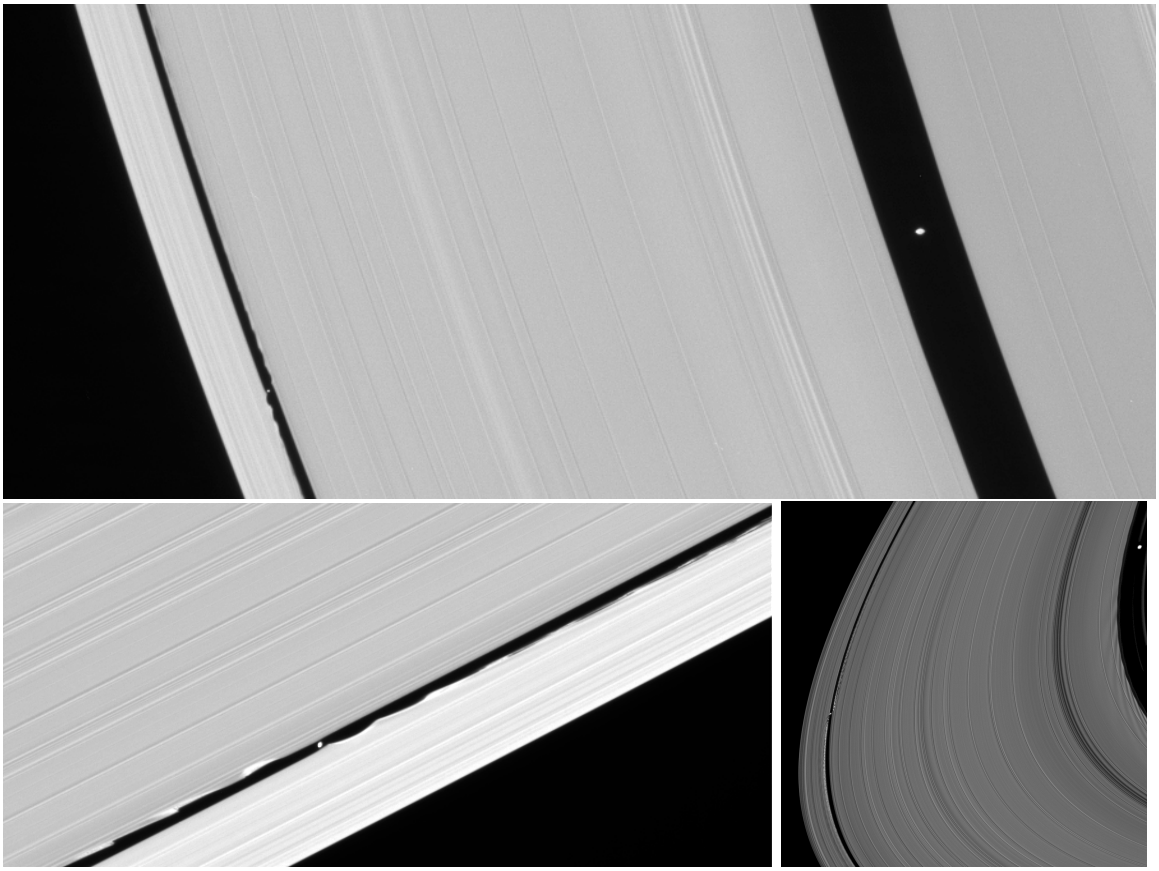

Figure 9: Structures in Saturn's A ring produced by nearby massive objects. Top: Overview of the outer A ring, showing the gaps surrounding the moons Pan (right) and Daphnis (left). Bottom left: Close-up of the disturbed ring material in the vicinity of Daphnis. Bottom right: A view of the moonlet wakes in the vicinity of both Pan and Dephnis. (NASA Planetary photojournal images PIA08926, PIA08319 and PIA14608

4.1 Local perturbations

The response of dense rings to nearby perturbers can be observed most clearly in the vicinity of two small moons called Pan and Daphnis that are actually embedded in Saturn's A ring (Figure 9). Both these moons orbit within nearly empty gaps in the A ring, and the material on either side of these gaps is clearly perturbed by the moons: the edges of the gaps appear wavy and there are periodic density variations known as "moonlet wakes" extending into the ring material.

The response of the ring material is most easily calculated and understood using a coordinate system centered on the moon, which we will here assume to be on a circular orbit with a semi-major axis a_m. The moon's mass M_m will also be assumed to be much less than the planet's mass M_P (i.e. $M_m/M_P << 1$), and the ring particles' orbits are assumed to be co-planar with the moons. In this case, the particles' trajectories can be

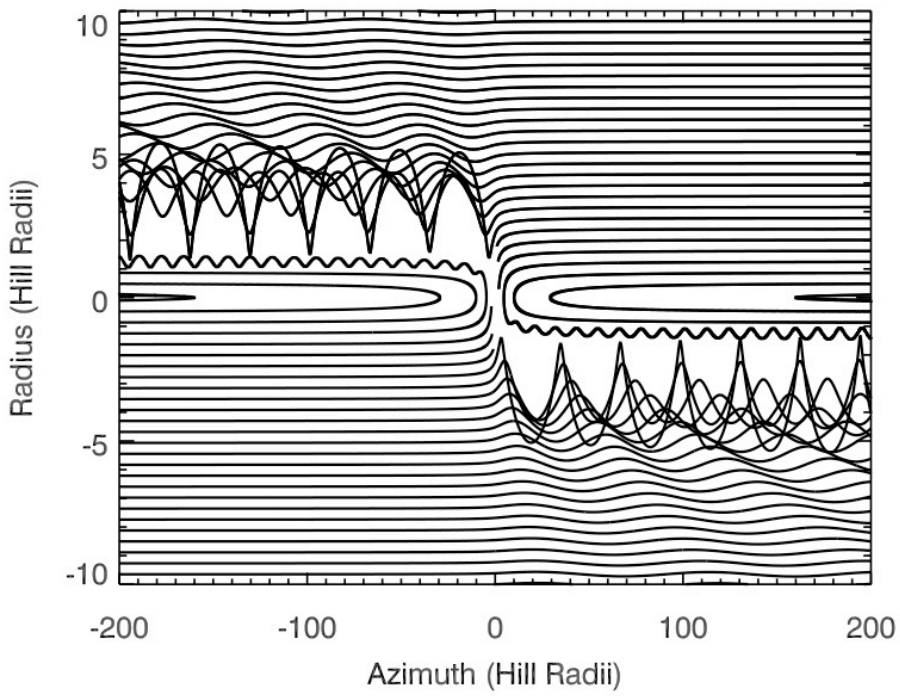

Figure 10: Trajectories of ring particles in the vicinity of a massive object. Radial and azimuthal distances are measured in units of the objects Hill radius $r_H = a(M_m/3M_P)^{1/3}$. Note particles approach the moon from the lower left and the upper right on nearly circular orbits. Figure adapted from Tiscareno *et al.* (2008).

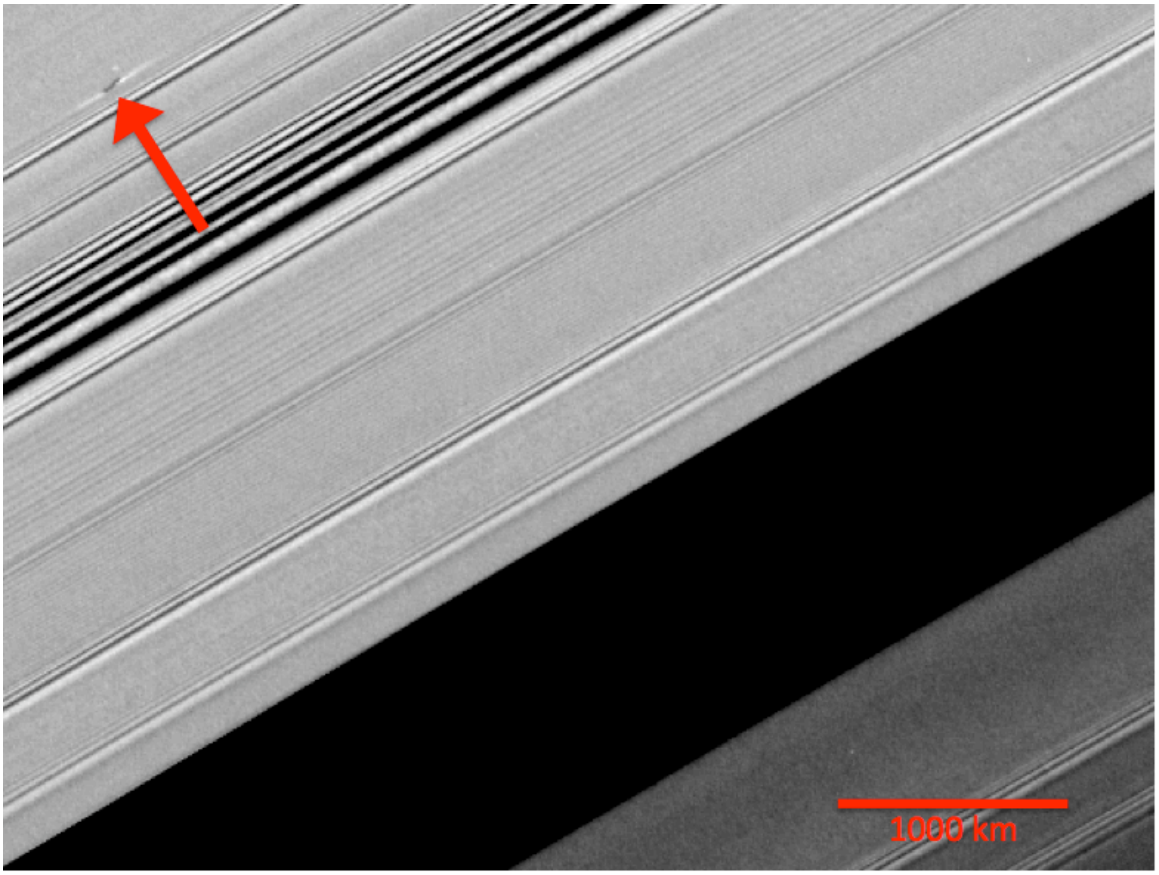

Figure 11: A propeller object in Saturn's A ring (highlighted by the red arrow). This object is a localized disturbance in the ring caused by an object that is larger than typical ring particles, but too small to open up a complete gap. (NASA Planetary Photojounral image PIA12791)

computed using the approximate equations of motion known as Hill's equations:

$$\ddot{x} - 2n\dot{y} = \left(3 - \frac{M_m}{M_p}\frac{a_m^3}{(x^2+y^2)^{3/2}}\right) n^2 x \tag{73}$$

$$\ddot{y} - 2n\dot{x} = -\left(\frac{M_m}{M_P}\frac{a_m^3}{(x^2+y^2)^{3/2}}\right) n^2 y \tag{74}$$

where x and y are Cartesian coordinates aligned with the radial and azimuthal directions, respectively. Figure 10 illustrates the computed trajectories for particles that approach the moon on initially circular orbits with a range of semi-major axes $a_m + \delta a$. This image shows that the moon's perturbations have different effects on the particles trajectories depending on the magnitude of $|\delta a|$ relative to a characteristic scale set by the mass of the moon known as the Hill radius $r_H = a(M_m/3M_P)^{1/3}$ (see also Murray and Dermott 1999).

Particles with semi-major axes within about two Hill radii of the moon's orbit approach the moon extremely slowly, and the moon's gravity tugs the particle mostly in the azimuthal direction, which actually prevents the material from ever getting too close to the moon. For example, consider a particle that is initially slightly closer to the planet than the moon, and therefore is moving slightly faster than the moon. As the particle approaches the moon from behind, it will feel a forward tug that accelerates it and causes its semi-major axis to increase. Eventually, the semi-major axis of the particle will exceed the semi-major axis of the moon, and the particle will start to drift backwards away from the moon. In principle, the moon can even catch up with this particle some time later, at which case the backwards tug of the moon will slow the particle's orbital motion and cause its orbit to decay inward again. The particle can therefore alternately drift back and forth around the moon's orbit, producing something called "horseshoe motion" because the particle's trajectory looks like a horseshoe in a reference frame where both the moon and planet are fixed. A faint ringlet that lies near the orbit of Pan may consist of material executing these sorts of horseshoe motions.

Particles more than a few Hill radii from the moon's semi-major axis show very different behaviors. These particles can actually drift past the moon, and the moon's gravitational perturbation can be well approximated as an impulsive event where the particle is briefly pulled towards the moon's orbit during conjunction. Such a perturbation gives each particle a finite eccentricity e, which causes the particle to alternately approach and recede from the moon's orbit as they proceed away from the moon, giving rise to the wavy trajectories seen in Figure 10 (see also Murray and Dermott 1999). Since the particles drift past the moon at a speed $V_{\rm rel} = -(3/2)n\delta a$, and the local orbit period is $2\pi/n$, these wave-like trajectories have a characteristic wavelength of $3\pi|\delta a|$. This matches the observed wavelengths of the wavy edges seen on either side of Daphnis in Figure 9 (see Weiss *et al.* 2009 and references therein).

All the particles in these regions start out with aligned pericenters, but since the wavelength depends on the semi-major axis separation $|\delta a|$, the radial motions eventually get out of step, leading to variations in the typical distances between the streamlines

and thus variations in the local surface density known as moonlet wakes. Such density variations can in fact be observed along the edges of gaps carved by the moons Pan and Daphnis in Saturns A ring (see Figure 9). Further downstream, the trajectories of particles actually cross, and this should in principle lead to dissipation of coherent patterns and to the ring particles again having circular orbits on average. However, while this does appear to be the case for the wakes around Daphnis, the wake patterns generated by Pan do not dissipate quickly, and in fact it appears that the wakes persist more that 360° downstream of Pan (Tiscareno *et al.* 2007 and references therein).

In addition to inducing eccentricities, these encounters also produce important changes in the particles' semi-major axes. In order for the moon to change a particle's semi-major axis, the moon must exert a net azimuthal force as the particle drifts by the moon (see Section 2 above). If the particle's orbit remained perfectly circular as it passed by the moon, the azimuthal component of the force before and after the encounter would cancel each other out, and no change in semi-major axis would occur. However, if the particle is on a circular orbit before it encounters the moon and is on an eccentric one afterwards, then the particle is slightly closer to the moon after the encounter than it was before the encounter, and the net azimuthal force is not exactly zero. The net azimuthal force always pulls the particle back towards the moon after the encounter, which causes the particles' semi-major axes to move away from the moon's orbit. For example, if the particle's orbit is interior to that of the moon, the net force acts to slow the particles orbital motion, causing it to fall inwards, away from the moons orbit. This process, known as gravitational shepherding, allows the gravitational tugs from the moons to counteract the natural tendency of the ring material to spread, and thus maintains the gaps in their vicinity. Similar processes may play a role in confining material in narrow ringlets, such as Uranus' ϵ ring, which is surrounded by the small moons Cordelia and Ophelia (see Borderies *et al.* 1989, Dermott 1984, Murray and Dermott 1999 and references therein).

Recently, high-resolution images of Saturn's rings obtained by the Cassini spacecraft has revealed the existence of localized disturbances known as "propellers", consisting of two streaks extending in opposite directions from a central core (see Figure 11). The two arms are slightly displaced in radius, consistent with the regions of maximal disturbance around a massive object shown in Figure 10. These features are therefore interpreted as the signatures of objects large enough to disturb ring material in their vicinity, but too small to open a gap (Tiscareno *et al.* 2006, 2008, Sremečević *et al.* 2007). Some of these objects can be tracked over periods of years, and exhibit non-keplerian motions that may reflect interactions between the massive object and the disk of ring particles (Tiscareno *et al.* 2010).

4.2 Resonant perturbations

In addition to the structures produced by massive objects embedded within the rings, Saturn's A ring also possesses numerous structures generated by resonances with more distant moons. Resonant perturbations on dense rings are responsible for such diverse features as spiral bending waves, spiral density waves, and resonantly confined ring edges.

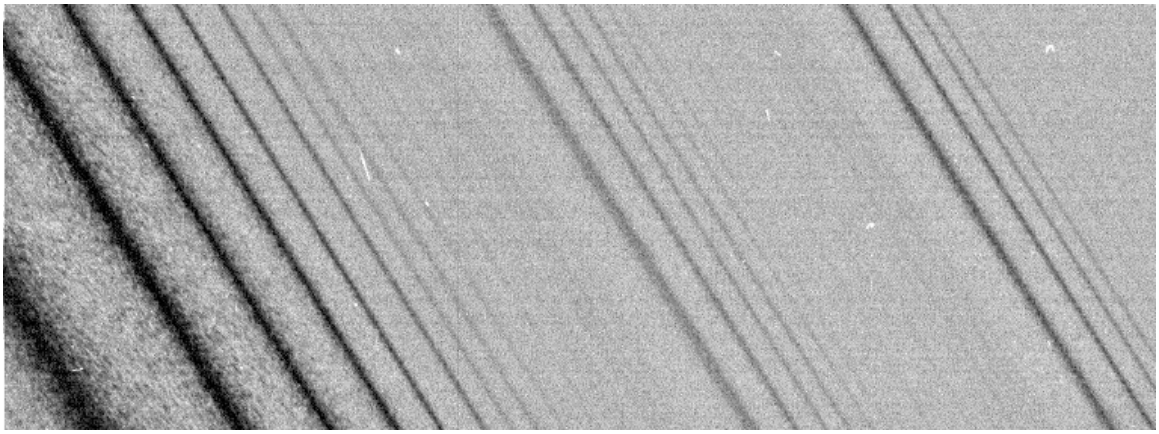

Figure 12: Density waves in Saturn's A ring, as observed by Cassini. Radius increases to the upper right, and each quasi-periodic variation in brightness corresponds to the location of a particular Lindblad resonance with one of Saturn's moons. (NASA Planetary Photojournal image PIA06095)

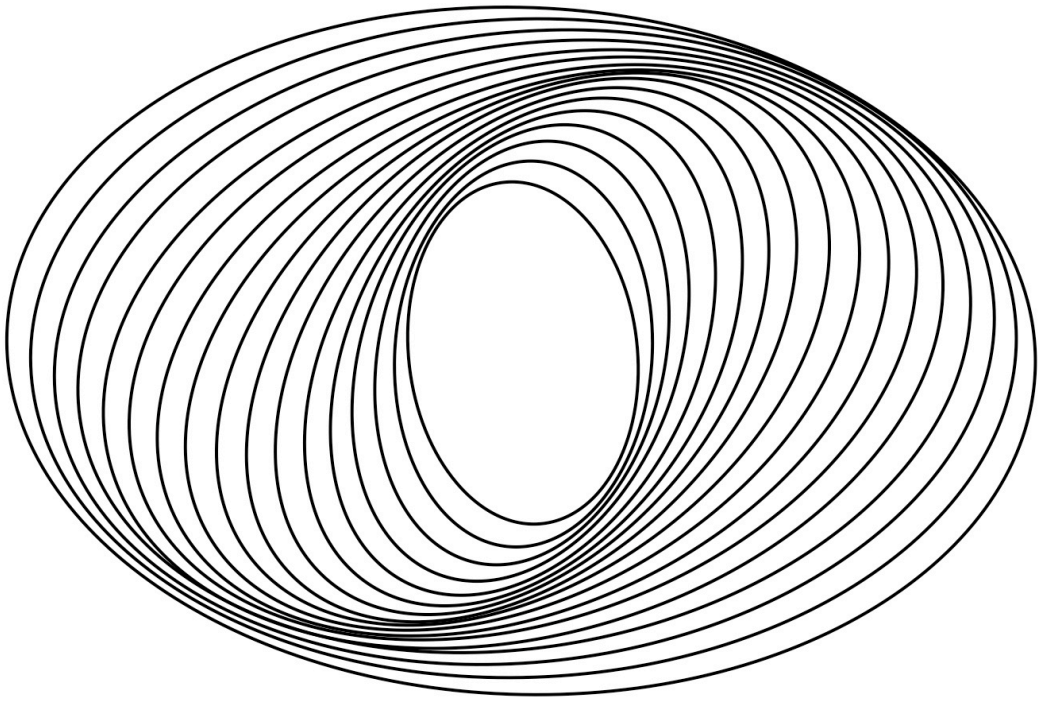

Figure 13: Cartoon representation of a $j = 2$ density wave. Each line shows the streamline trajectory of particles at different semi-major axes. Note the patterns are much more tightly wound in a real density wave than shown here.

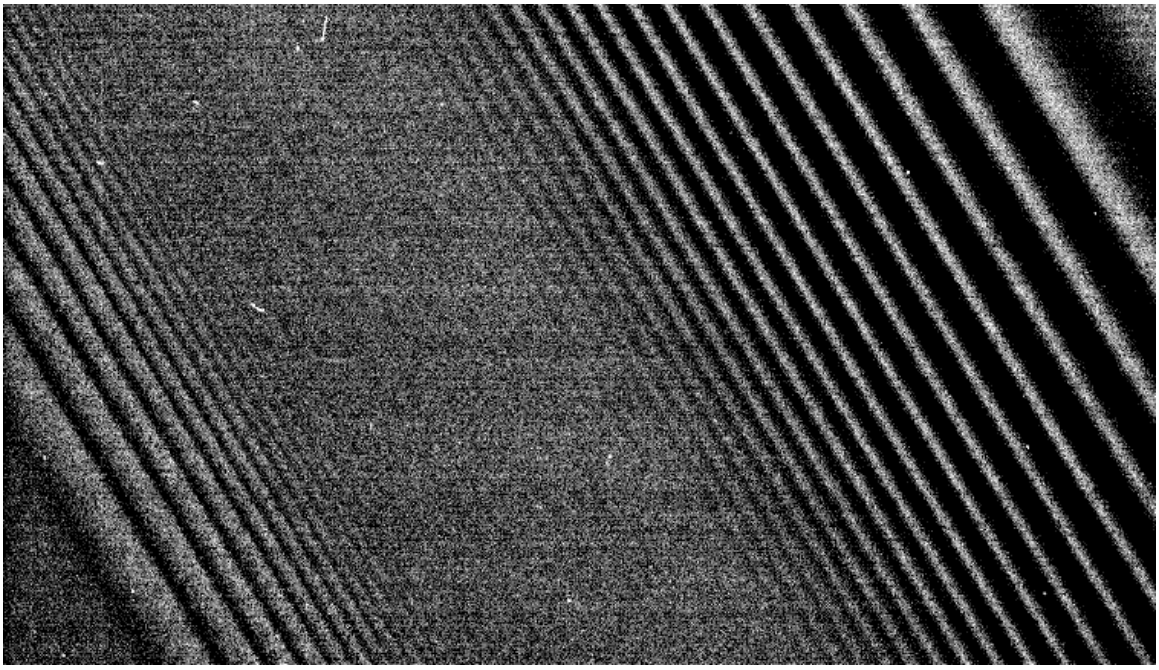

Figure 14: Close-up image of Saturn's A ring taken by the Cassini spacecraft, showing a density wave (left) and a bending wave (right). Radius increases to the upper right. (NASA Planetary Photojournal image PIA06093),

The theory behind these various features is somewhat involved and is already discussed in great detail in the existing literature (see Goldreich and Tremaine 1982 and Shu 1984), so here we will only give a very brief and qualitative overview of the basic physics involved in the formation of these features.

Figure 12 is an image of three spiral density waves in Saturn's A ring, where the observed brightness variations reflect modulations in the ring's surface density. Each one of the features occurs at a first-order Lindblad resonance with one of Saturn's moons. As discussed above, first-order Lindblad resonances induce forced eccentricities in ring particles, giving rise to patterns that have a symmetry determined by the resonance and that remain fixed with respect to the perturbing moon (see Figure 5). However, the forced eccentricities induced by the resonance are only periodic in the azimuthal direction, and do not create periodic radial structures like those seen in Figure 12. The observed patterns are therefore not generated directly by the resonance, but are instead a tightly wound spiral pattern analogous to that shown in Figure 13.

The spiral pattern of these features arises from the mutual gravitational interactions among the various particles in the ring. Like the pattern shown in Figure 5, the pattern shown in Figure 13 does not rotate around the planet at the local orbital rate n, but instead rotates at a pattern speed n_P equivalent to the mean motion of the relevant perturbing moon. Each ring particle therefore moves through this pattern, and feels a periodic perturbing force as it moves past regions of different densities. These periodic

perturbations induce forced eccentricities with organized pericenters similar to those of other particles in their vicinity, creating a self-reinforcing pattern of streamlines and density variations that moves around the planet at a single rate.

The basic characteristics of these spiral density waves are encoded in the following dispersion relation, which is derived in Shu 1984:

$$(jn_P - jn)^2 - (n - \dot{\varpi}_0)^2 = -2\pi G\Sigma|k_r| \tag{75}$$

where n_P is the pattern speed, j is the number of arms in the spiral pattern, $\dot{\varpi}_0$ is the free precession rate due to the planets finite oblatenes (given by Equation 19 above), Σ is the ring's average (unperturbed) surface mass density and k_r is the radial wavenumber of the wave (i.e. 2π over the radial wavelength). Note that at the exact resonance, the left-hand side of this equation is precisely zero, and so the pattern has $k_r = 0$ and the density variations are purely azimuthal. Interior to the resonance, the left hand side of this equation becomes positive so no real value of k_r is allowed, but outside the resonance the left hand side becomes increasingly negative, so the wave can have real radial wavelength that becomes progressively shorter with distance from the resonance. This is consistent with the patterns seen in Figure 12 and 13, which become tighter with increasing radius. Furthermore, since the rate at which the wavenumber increases with distance from the resonance depends on the surface mass density of the ring, these features have been extremely useful tools for estimating the local surface mass density of the rings (see Colwell *et al.* 2009 and references therein).

As the spiral pattern becomes more tightly wound further from the resonance, the streamlines will crowd closer and closer together and the density variations will become larger and larger. Indeed, the patterns shown in Figure 12 are most intense some distance downstream from the resonance, where the radial wavenumber of the spiral pattern is finite. However, even further from the resonance, the pattern fades and eventually disappears. This is because the random motions of the particles in the ring eventually dissipate the coherent motions associated with the wave. Indeed, the radial extents of these waves can constrain the velocity dispersions and local effective viscosities of these rings (again, see Colwell *et al.* 2009).

In addition to density waves generated by Lindblad resonances, there are also bending waves generated by vertical resonances. These features again can appear as periodic brightness variations in images (see Figure 14), but they actually represent oscillations in the rings vertical position, which lead to differences in the amount of material along the line of sight. These vertical warps are again organized into tightly wound spiral patterns, which are governed by the dispersion relation (Shu 1984):

$$(jn_P - jn)^2 - (n - \dot{\Omega}_0)^2 = +2\pi G\Sigma|k_r| \tag{76}$$

where $\dot{\Omega}_0$ in the free nodal precession rate given by equation 20 above. Note the opposite sign on the right-hand side compared with the previous equation, which implies that these patterns can only have real finite wavenumbers interior to the resonance. Indeed, the bending wave in Figure 14 propagates in the opposite direction as the density wave.

Finally, we may briefly note that resonances with distant moons are also responsible for the sharp outer edges of both Saturns A and B rings. Much like the gap edges produced by nearby moons discussed above, the resonant torques from a moon at a strong resonance can counteract the natural tendency of the ring to spread (Bordereis *et al.* 1982, 1989, Hahn *et al.* 2009). The importance of such resonances in controlling these edges is clearly demonstrated by the observed variations in the positions of these edges, which have components with azimuthal wavenumbers and pattern speeds consistent with those that would be generated by the eccentricities forced by the appropriate resonance. However, there are other radial variations on these edges as well, indicating that the dynamics of these sharp edges are more complex than some had expected (Spitale and Porco 2009, 2010, Hedman *et al.* 2010b).

5 Conclusions

Planetary rings are exceptionally rich and dynamic particle systems, exhibiting structures on a wide range of scales involving a great diversity of processes such as collisions, gravitational forces and non-gravitational perturbations. Since these same basic processes operate in many other astrophysical systems, including spiral galaxies and protoplanetary disks, the insights gained from detailed studies of planetary rings have the potential to illuminate the dynamics of many other astronomical phenomena.

Acknowledgements

I wish to thank J.A. Burns, P.D. Nicholson, M.S. Tiscareno and H. Salo for their comments and useful conversations that helped me to better understand some of the topics covered in this chapter.

Glossary

Bending wave or spiral bending wave: A periodic modulation in the vertical position of a dense ring that is generated by a vertical resonance.

Co-rotation eccentricity resonance: A mean-motion resonance in which the resonant argument includes the pericenter location of the perturbing moon. These sorts of resonances can confine material at particular co-rotating longitudes.

Density wave or spiral density wave: A periodic pattern of density variations in a dense ring that is generated by a Lindblad resonance.

Dynamical optical depth: A standard measure of the average number of particles per unit surface area in the rings. While this number is directly related to the rings' surface mass density, it does not necessarily equal the rings' observed optical depth.

Table 1: Symbols used in this chapter

B	elevation angle above rings
D_2	average surface number density of ring particles
F_D	azimuthal drag force
F_G	central gravitational force from planet, $GM_P m/a^2$
F_I	inertially fixed force
F_m	gravitational force from a moon
F_r	radial component of perturbing force
F_z	vertical component of perturbing force
F_λ	azimuthal component of perturbing force
G	gravitational constant
H	ring vertical thickness
J_2	planetary oblateness parameter
M_P	planet mass
M_m	moon mass
R	planet radius
T	ring transmission coefficient
U	gravitational potential
V_r	average radial velocity of ring particles
V_z	average vertical velocity of ring particles
V_λ	average azimuthal velocity of ring particles
a	orbital semi-major axis
a_m	moon's orbital semi-major axis
c	root-man-square velocity dispersion
c_z	vertical rms velocity dispersion
e	orbital eccentricity
e_f	forced eccentricity
e_l	free eccentricity
e_m	moon's eccentricity
f	true anomaly
i	orbital inclination
i_m	moon's inclination
h	$e\cos(\varpi - \lambda_0)$
k	$e\sin(\varpi - \lambda_0)$
k_r	radial wavenumber
m	ring particle mass
n	orbital mean motion
n_P	pattern speed
r	radial distance from planet's spin axis
r_H	Hill radius
r_R	Roche limit
s	ring particle radius
u_r	random radial velocity of ring particles
u_z	random vertical velocity of ring particles
u_λ	random azimuthal velocity of ring particles
v_r	radial velocity of ring particles
v_z	vertical velocity of ring particles
v_λ	azimuthal velocity of ring particles
x	cartesian approximation of radial coordinate
y	cartesian approximation of azimuthal coordinate
z	vertical displacement above ring-plane
ϵ	eccentric anomaly (equation 3 only)
ϵ	coefficient of restitution
λ	inertial longitude
λ_0	reference longitude
λ_T	Toomre critical wavelength
$\nu_{\rm eff}$	effective kinematic shear viscosity
ρ	ring particle mass density
$\rho_{\rm crit}$	Roche critical density
ρ_P	planet mass density
Σ	ring surface mass density
τ	ring optical depth
τ_D	dynamical optical depth
φ_{CR}	resonant argument of a corotation resonance
φ_{LR}	resonant argument of a Lindblad resonance
φ_{VR}	resonant argument of a vertical resonance
ω	argument of pericenter
ω_c	collision frequency
ϖ	longitude of pericenter
ϖ_m	moon's longitude of pericenter
$\dot{\varpi}_0$	free apsidal precession rate
Ω	longitude of ascending node
Ω_m	moon's longitude of ascending node
$\dot{\Omega}_0$	free nodal regression rate

Gravitational shepherding: The process whereby the gravitational torques from a nearby moon prevent ring material from viscously spreading.

Hill radius: A natural distance scale that arises in the circular restricted three body problem that contains a planet, a moon on a circular orbit, and a massless test particle. The moon's Hill radius determines its gravitational sphere of influence.

Horseshoe motion: A type of orbital motion that can occur in the three body problem, where a small particle alternately drifts forwards and backwards in longitude relative to the moon.

Lindblad resonance: A mean-motion resonance in which the resonant argument includes the pericenter location of the ring particle. These sorts of resonances tend to induce finite eccentricities in the ring-particles' orbits.

Moonlet wakes: Density variations in a ring produced by the gravitational perturbations from a nearby moon.

Normal optical depth: The optical depth that would be measured if the light passed perpendicularly through the rings.

Optical depth: Standard measure of ring opacity computed from the observed transmission coefficient T using the expression $\tau = -\ln(T)$.

Overstability: A phenomenon whereby the amplitude of a small oscillation grows over time. May occur in some parts of Saturn's dense rings.

Propellor: A localized disturbance in the ring produced by an embedded object that is larger than the typical ring particle but too small to open up a complete gap in the rings.

Roche limit: A critical distance from the center of a planet where an object can just barely maintain its integrity against tidal forces. This distance depends on the mass density of the object. Dense rings are most likely to be found inside this critical distance.

Roche critical density: The minimum density at a given distance from the planet which would allow an object to maintain its integrity against tidal disruption.

Self-gravity wakes: Transient, elongated agglomerations of ring particles that arise due to the combination of ring-particles' mutual gravitational attraction and keplerian shear.

Toomre critical wavelength: The largest unstable wavelength in a shearing disk. Determines the wavelength of self-gravity wakes.

Transmission coefficient: The fraction of light that passes through a ring without being scattered or absorbed.

Vertical resonance: A mean-motion resonance in which the resonant argument includes the ascending node longitude of the ring particle. These sorts of resonances tend to induce

finite inclinations in the ring-particles' orbits.

Bibliography

Borderies, N. P. Goldreich and S. Tremaine. 1982. Sharp edges of planetary rings. *Nature* Vol 299 pp 209-211.

Borderies, N. P. Goldreich and S. Tremaine. 1989. The formation of sharp edges in planetary rings by nearby satellites. *Icarus* Vol 80 pp 344-360.

Bridges, F.G. A. Hatzes and D. Lin. 1984. Structure, stability and evolution of Saturns rings. *Nature* Vol 309, pp. 333-335.

Burns, J.A. 1976. Elementary derivation of the perturbation equations of celestial mechanics. *American Journal of Physics.* Vol. 44 pp 944-949 (plus erratum in Vol 45 pp 1230) [Provides a good heuristic derivation of the perturbation equations for the various orbital elements.]

Burns, J.A., P.L. Lamy and S. Soter. 1979. Radiation forces on small particles in the Solar System. *Icarus.* Vol 40, pp 1-48. [A useful overview of some of the non-gravitational forces that can influence the orbital dynamics of small particles in planetary rings.]

Burns, J.A. L.E. Schaffer R.J. Greenberg and M.R. Showalter. 1985. Lorentz resonances and the structure of the Jovian ring. *Nature*. Vol 316 pp 115-119.

Burns J.A. M.R. Showalter D.P. Hamilton P.D. Nicholson I. de Pater M.E. Ockert-Bell and P.C. Thomas. 1999. The formation of Jupiter's faint rings. *Science*. Vol 284 pp 1146-1150.

Burns, J.A. D.P. Simonelli M.R. Showalter D.P. Hamilton C.C. Porco and H. Throop. 2004. Jupiter's ring-moon system. Bagenal F., T.E. Dowling and W.B. McKinnon (eds). *Jupiter: The Planet Satellites and Magnetosphere*. Cambridge, Cambridge Univ. Press. pp 241-262. [A recent overview of the structure, composition and dynamics of Jupiter's ring system.]

Charnoz, S. A. Brahic P.C. Thomas and C.C. Porco. 2007. The equatorial ridges of Pan and Atlas: Terminal acccreetionary ornaments? *Science*. Vol 318 pp 1622-1624.

Charnoz, S. L. Dones, L.W. Esposito P.R. Estrada and M.M. Hedman. 2009. The origin and evolution of Saturns ring system. Doughertry, M.K., L.W. Esposito, and S.M. Krimigis (eds). *Saturn from Cassini Huygens*. New York, Springer. pp 375-413. [A good review of processes relevant to the long-term evolution of dense ring systems.]

Charnoz, S. J. Salmon and A. Crida. 2010. The recent formation of Saturn's rings from viscous spreading of the main rings. *Nature*. Vol 465. pp 752-754.

Colwell, J.E. L.W. Esposito M. Sremčević and G.R. McClintock. 2007. Self-gravity wakes and radial strucure os Saturn's B ring *Icarus*. Vol 200 p 574-580.

Colwell, J.E. P.D. Nicholson M.S. Tiscareno C.D. Murray R.G. French and E.A. Marouf. 2009. The structure of Saturns rings. Doughertry, M.K., L.W. Esposito, and S.M. Krimigis (eds). *Saturn from Cassini Huygens*. New York, Springer. pp 375-413. [A recent overview of the observed structures in Saturn's dense rings, including the A, B, C and F rings.]

Cuzzi, J. R. Clark G. Filacchione R. French R. Johnson E. Marouf and L. Spilker. 2009. Ring particle composition and size distribution. Doughertry, M.K., L.W. Esposito, and S.M. Krimigsi (eds). *Saturn from Cassini Huygens*. New York, Springer. pp 459-509. [A good recent overview of the available constraints on the particle size distribution and material composition of Saturn's rings.]

Dermott, S.F. 1984. Dynamics of Narrow Rings. R. Greenberg and A. Brahic (eds) Planetary Rings. Tuscon, University of Arizona Press. pp. 589-639.

de Pater, I. S.G. Gibbard E. Chiang H.B. Hammel B. Macintosh F. Marchis S.C. Martin H.G. Roe and M. Showalter. 2005. The dynamic neptunian ring arcs: Evidence for a gradual disappearance of Liberte and resonant jump of Courage. *Icarus*. Vol 174 pp 446-454.

de Pater, I. S.G. Gibbard H.B. Hammel. 2006a. Evolution of the dusty rings of Uranus. *Icarus*. Vol. 180 pp 186-200.

de Pater, I. H.B. Hammel S.G. Gibbard M.R. Showalter. 2006b. New dust belts of Uranus: One ring, two ring, red ring, blue ring. *Science*. Vol. 317 pp 1888-1890.

Doughertry, M.K. L.W. Esposito, and S.M. Krimigis. 2009. *Saturn from Cassini Huygens*. New York, Springer. [A book that provides a general overview of the current state of knowledge of many aspects of the Saturn system, including Saturn's rings.]

Dumas, C. R.J. Terrile B.A. Smith G. Schneider and E.E. Becklin. 1999. Stability of Neptune's ring arcs in question. *Nature*, Vol 400 pp 733-735.

Esposito, L.W. A. Brahic J.A. Burns and E.A. Marouf. 1991. Partice properties and processes in Uranus' rings. Bergstralh, J.T. E.D. Miner and M.S. Matthews. *Uranus*. Tucson, University of Arizona Press. pp. 410-465. [The most recent overview of the particle size distribution and material composition of Uranus' rings.]

French, R.G. P.D. Nicholson, C.C. Porco and E.A. Marouf. 1991. Dynamics and structure of the Uranian rings. Bergstralh, J.T. E.D. Miner and M.S. Matthews. *Uranus*. Tucson, University of Arizona Press. pp. 327-409. [The most recent overview of the dynamical processes operating in Uranus' rings.]

Goldreich, P. and S. Tremaine. 1982. Dynamics of Planetary rings. *Ann. Rev. Astron. Astrophys.*. Vol 241. pp 425-441. [A good overview of some of the important dynamical processes that can operate in dense rings, including discussions of spiral waves.]

Greenberg, R. and A. Brahic. 1984. *Planetary Rings*. Tuscon, University of Arizona

Press. [A good book containing many chapters discussing the dynamics of planetary ring systems.]

Hahn, J.M. J.N. Spitale and C.C. Porco. 2009. Dynamics of the sharp edges of broad planetary rings. *ApJ.* Vol 699 pp 686-710.

Hedman, M.M. J.A. Burns M.S. Tiscareno C.C. Porco G.H. Jones E. Roussos N. Krupp C. Paranicas and S. Kempf. 2007. The source of Saturn's G ring. *Science.* Vol 317 pp 653-656.

Hedman M.M. J.A. Burns M.S. Tiscareno and C.C. Porco. 2009a. Organizing some very tenuous things, Lindblad resonances in Saturn's faint rings. *Icarus.* Vol 202 pp 260-279.

Hedman M.M. C.D. Murray, N.J. Cooper, M.S. Tiscareno, K. Buerle, M.W. Evans, J.A. Burns. 2009b. Three tenuous rings/arcs for three tiny moons *Icarus.* Vol 199 pp 378-286.

Hedman, M.M. J.A. Burt, J.A. Burns, M.S. Tiscareno. 2010a. The shape and dynamics of a heliotropic dusty ringlet in the Cassini Division. *Icarus.* Vol 210 pp 284-297.

Hedman, M.M. P.D. Nicholson, K.H. Baines B.J. Buratti C. Sotin R.N. Clark R.H. Brown R.G. French and E.A. Marouf. 2010b. The architecture of the Cassini Division. *AJ.* Vol 139 pp 228-251.

Horanyi, M. J.A. Burns M.M. Hedman G.H. Jones and S. Kempf 2009. Diffuse rings. Doughertry, M.K., L.W. Esposito, and S.M. Krimigis (eds). *Saturn from Cassini Huygens.* New York, Springer. pp 511-536. [The most recent review of the structure and dynamics of Saturn's faint, dusty rings, including the D. E and G rings.]

Julian, W.H. and A. Toomre. 1966. Non-axisymmetric responses of differentially rotating disks of stars. *ApJ.* Vol 146 pp 810.

Murray, C.D. and S.F. Dermott, 1999. *Solar System Dynamics.* New York, Cambridge University Press. [A very useful textbook on dynamical processes, which includes treatments of many dynamical phenomena that occur in dense rings.]

Namouni, F. and C.C. Porco. 2002. The confinement of Neptune's ring arcs by the moon Galatea. *Nature.* Vol 417 pp 45-47.

Nicholson, P.D. I. Mosquiera and K. Matthews. 1995. Stellar occultation observations of Neptune's rings: 1984-1988. *Icarus.* Vol 113 pp 295-330.

Porco, C.C. 1991. An explanation for Neptune's ring arcs. *Science.* Vol 253 pp 995-1001.

Porco, C.C. P.D. Nicholson J.N. Cuzzi J.J. Lissauer and L.W. Esposito. 1995. Neptune's ring system. Cruikshank, D.P. (ed). *Neptune and Triton* Tuscon, University of Arizona Press. pp 703-804. [The most recent review of the structure and dynamics of Neptune's ring system.]

Porco, C.C. P.C.Thomas J.W. Weiss and D.C. Richardson. 2007. Saturn's small satellites: Clues to their origins. *Science.* Vol. 318 pp 1602-1607.

Robbins, S.J. G.R. Stewart M.C. Lewis J.E. Colwell and M. Sremčević. 2010. Estimating the masses of Saturn's A and B rings fro high-optical depth N-body simulations and stellar occultations. *Icarus*. Vol 206 pp431-445.

Salo, H. 2001. Numerical simulations of the collisional dynamics of planetary rings. *Lecture Notes in Physics* Vol 564 pp 330.

Salo, H. R. Karjalainen and R.G. French. 2004. Photometric modeling of Saturn's rings II. Azimuthal asymmetry in reflected and transmitted light. *Icarus.* Vol 170 pp 70-90.

Schmidt, J. K. Ohtsuki N. Rappaport H. Salo and F. Sphan 2009. Dynamics of Saturns dense rings. Doughertry, M.K., L.W. Esposito, and S.M. Krimigis (eds). *Saturn from Cassini Huygens.* New York, Springer. pp 413-458. [A good discussion of many aspects of the dynamics of dense rings, especially inter-particle interactions]

Shu, F. 1984. Waves in planetary rings. R. Greenberg and A. Brahic (eds) *Planetary Rings.* Tuscon, University of Arizona Press. pp. 513-561. [The classic reference on the dynamics of spiral waves in dense rings.]

Sicardy, B. F. Roddier C. Roddier E. Perozzi J.E. Graves O. Guyon and M.J. Northcott. 1999. Images of Neptune's ring arcs obtained by a ground-based telescope. *Nature*. Vol 400 pp 731-733.

Spitale, J.N. and C.C. Porco. 2009. Time variability in the outer edge of Saturn's A-ring revelaed by Cassini imaging. *AJ.* Vol 138 pp 1520-1523.

Spitale, J.N. and C.C. Porco 2010. Detection of free unstable modes and massive bodies in Saturn's outer B ring. *AJ.* Vol 140 pp 1747-1757.

Sremčević, M. J.Schmidt, H. Salo, M. Siess, F. Spahn and N. Albers. 2007. A belt of moonlets in Saturn's A ring. *Nature*. Vol 449 pp 1019-1021.

Thomson, F.S. E.A. Marouf G.L. Tyler R.G. French and N.J. Rappaport. 2007. Periodic microstructures in Saturn's rings A and B. *GRL.* Vol 34 L24,203.

Tiscareno, M. S. 2012 Planetary Rings. L. French and P. Kalas(ed.), *Solar and Planetary Systems.* Springer (arXiv 1112.3305) [A recent chapter reviewing the current state of knowledge of various planetary rings. Includes a particularly interesting discussion of the Roche limit in these systems.]

Tiscareno M.S. J.A. Burns M.M. Hedman C.C. Porco J.W. Weiss L. Dones D.C. Richardson and C.D. Murray. 2006. 100-meter-diameter moonlets in Saturn's A ring from observations of "propeller" structures. *Nature.* Vol 440 pp 648-650.

Tiscareno, M.S. J.A. Burns P.D. Nicholson M.M. Hedman and C.C. Porco. 2007. Cassini imaging of Saturn's rings II. A wavelet technique for analysis of density waves and other radial structures in the rings. *Icarus*. Vol 189, 14-34.

Tiscareno, M.S. J.A. Burns M.M. Hedman and C.C. Porco. 2008. The population of

propellors in Saturn's A ring. *AJ.* Vol 135 pp 1983-1091.

Tiscareno, M.S. *et al.* 2010. Physical characteristics and non-keplerian orbital motion of "propeller" moons embedded in Saturn's rings. *ApJL.* Vo 718 pp L92-96.

Tremaine, S. 2003. On the origin of irregular structure in Saturn's rings. *AJ.* Vol 125 pp 894-901.

Verbiscer A.J. M.F. Skrutskie and D.P. Hamilton. 2009. Saturn's largest ring. *Science.* Vol 461 pp 1098-1100.

Weiss, J.W. C.C. Porco and M.S. Tiscareno. 2009. Ring edge waves and the masses of nearby satellites. *AJ.* Vol 138 pp 272-286.

Biographical Sketch

Matthew Hedman (born in 1974 in St. Paul, Minnesota, USA) is a research associate at Cornell University. For the last seven years, he has been working for the Cassini Mission to Saturn on a variety of efforts to understand the structure, composition and dynamics of Saturn's rings.